TAMPEREEN TEKNILLINEN YLIOPISTO
TAMPERE UNIVERSITY OF TECHNOLOGY

Roni Luhtala

Adaptive Control of Grid-Connected Inverters

Master of Science Thesis

Examiners: Academy Research Fellow Tomi Roinila, Assistant Prof. Tuomas Messo
Examiners and topic approved by the Faculty Council of the Faculty of Computing and Electrical-Engineering on the 1st of March 2017

Abstract

RONI LUHTALA: Adaptive Control of Grid-Connected Inverters
Tampere University of Technology
Master of Science Thesis, 69 pages
May 2017
Master's Degree Programme in Computing and Electrical-Engineering
Major: Power Electronics
Examiners: Academy Research Fellow Tomi Roinila, Assistant Prof. Tuomas Messo

Keywords: grid-connected inverter, adaptive control, impedance-based stability analysis, PRBS

Renewable energy resources are most often connected to the power grid through inverters. When significant amount of energy is produced by renewable energy resources the grid conditions vary faster than in conventional power system. Conventional power system was compromised of big synchronous generators which had sufficient amount of inertia to keep power quality and grid conditions close to constant. Today, novel techniques are required to guarantee power quality in varying grid conditions.

The inverter and grid can be modeled as an interconnected system. Stability of the interconnected system is considered often by the ratio of grid impedance and inverter output impedance. The grid impedance affects the inverter operation, and the inverter control system should adapt to these changes to ensure power quality.

In the work, adaptive controller is applied to optimize the operation of grid-connected inverter under varying grid conditions. In the method, the parameters of inverter grid synchronization are used, and the inverter controller is continuously updated to obtain desired operation. The adaptive controller is based on real-time measurement of grid impedance. The impedance measurement is carried out by applying pseudo-random binary sequence (PRBS) and Fourier techniques. The methods provide the impedance measurements in a fraction of time compared to most conventional measurement techniques.

The work presents an effective power-hardware-in-the-loop (PHIL) method that combines real-time online grid-impedance measurement system and adaptive control of grid-connected inverter. Experimental results based on a three-phase grid-connected inverter and grid are presented to demonstrate the effectiveness of the proposed methods.

Tiivistelmä

RONI LUHTALA: Verkkoon kytkettyjen vaihtosuuntaajien sopeutuva säätö
Tampereen teknillinen yliopisto
Diplomityö, 69 sivua
Toukokuu 2017
Sähkötekniikan diplomi-insinöörin tutkinto-ohjelma
Pääaine: Tehoelektroniikka
Tarkastajat: Akatemiatutkija Tomi Roinila, Assistant Prof. Tuomas Messo

Avainsanat: verkkoon kytketty vaihtosuuntaaja, PRBS, sopeutuva säätö, impedanssipohjainen stabiiliusanalyysi

Lisääntyvissä määrin käytetty uusiutuva energia kytketään useimmin sähköverkkoon vaihtosuuntaajan avulla. Uusiutuvien energialähteiden lisääntyessä verkon olosuhteet muuttuvat nopeammin ja täten vaihtosuuntaajien on säilytettävä riittävä sähkönlaatu muuttuvissa olosuhteissa. Tämänkaltaisen systeemin stabiiliutta voidaan tutkia impedanssipohjaisen stabiiliusanalyysin avulla vertailemalla verkon ja vaihtosuuntaajan impedansseja keskenään. Täten verkon olosuhteita vaihtosuuntaajan näkökulmasta voidaan kuvata impedanssina, jolla on vaikutusta vaihtosuuntaajan toimintaan ja systeemin stabiiliuteen. Vaihtosuuntaajan säätö voidaan kuitenkin sopeuttaa vallitseviin olosuhteisiin muuttamalla sen parametreja automaattisesti verkon impedanssimittauksiin perustuen siten, että vaihtosuuntaajan impedanssi muokkautuu yhteensopivaksi verkon impedanssin kanssa. Tämänkaltainen sopeutuva säätöjärjestelmä toteutettiin vaihtosuuntaajan verkkosynkronoinnin yhteydessä perustuen reaaliaikaiseenn verkon impedanssin mittaukseenn. Tulokset olivat oletetun kaltaisia ja paransivat sähkönlaatua merkittävästi etenkin hyvin äärimmäisissä olosuhteissa. Automaattisesti sopeutuvan säädön ansiosta myös mahdollinen irtikytkeytyminen verkosta voitiin estää tehokkaasti.

Preface

First I would like to thank my examiners Tomi Roinila and Tuomas Messo for very interesting topic for my Master of science thesis. I am also grateful of guidance in various problems during the research. Before starting to work with you, I did not even know the phrases like 'PRBS' or 'negative resistance'. Nowadays they are quite familiar for me and my expertise in field of power electronics is much higher level than I could even imagine before this great opportunity to research this topic with you.

I would also like to thank my wonderful family for love in every moment and for making my life meaningful. It is much easier to focus on work and education when the everyday life does not cause stress and you know that there is always someone taking care of you.

Also my great colleagues deserve praise for helping me countless times during this work and for interesting (usually off-topic) conversations. Without you it would have been much more stressful and boring to come to the office at the mornings. You also kept the operating conditions in the office at the level in which the total instability of the brain waveforms was absolutely impossible.

Tampere, 23rd May 2017

Roni Luhtala

Contents

Symbols

a	Amplitude of MLBS
C	Capacitance
C_f	Filter capacitor
d	Duty ratio
D	Steady-state of the duty ratio
Δt	Clock pulse interval
f	Frequency
f_{gen}	Generating frequency
f_r	Resonating frequency
f_{sw}	Switching frequency
G	System transfer function
G_{PI}	PI-controller of current control
$G_{\text{PI-dc}}$	PI-controller of DC-voltage control
$G_{\text{PI-PLL}}$	PI-controller of the PLL
H_{LCL}	Transfer function of LCL-filter
i	Current
I	Steady-state of the current
j	Imaginary component
K	Gain
K_i	Integral gain
K_p	Proportional gain
L	Inductance
L_f	Filter inductor
L_g	Grid inductance
L_{in}	DC-voltage control loop gain
L_{extra}	Extra inductance
L_{out}	Current control loop gain
L_{PLL}	PLL loop gain
L_t	Inductance of isolation transformer
M	Magnitude
n	Length of shift register
N	Length of the MLBS
P	Number of measured periods
$\mathbf{p}$	Real power
$p(s)$	Characteristic polynomial
$\mathbf{q}$	Reactive power

r_e	Equivalent resistance
R_f	Resistance of filter
R_g	Grid resistance
s	Laplace variable
$\mathbf{s}$	Apparent power
S_1	Relay
t	Time
T	Transmittance
t_{meas}	Measurement time
T_{MLBS}	MLBS period
θ	Phase shift
$\mathbf{u}$	Input vector
v	Voltage
V	Steady-state of the voltage
ω	Angular frequency
ω_p	Angular frequency of pole
ω_{PLL}	PLL bandwidth
ω_r	Resonating angular frequency
ω_s	Fundamental angular frequency
ω_z	Angular frequency of zero
Ω_Δ	Steady state phase difference
x	Signal in general
$X(\omega)$	Frequency domain excitation signal
X	Steady-state of the signal
X_g	Grid reactance
$\mathbf{x}$	State variable vector
$\mathbf{y}$	Output vector
Y	Admittance
$Y(\omega)$	Frequency domain output signal
Y_C	Filter admittance
Z	Impedance
Z_g	Grid impedance
Z_L	Load Impedance
Z_s	Source impedance
Φ_{MLBS}	Power spectrum of MLBS

Upper Index

$\hat{x}$	Averaged value
$x^{'}$	Sensed value
x^{*}	Reference value

Lower Index

x_{abs}	Three-phase in time-domain
$x_{\alpha\beta}$	$\alpha\beta$ -domain
x_{c}	Control-based
x_{C}	Variable based on capacitor
x_{-cl}	Closed loop
x_{d}	D-component
x_{dq}	Dq-domain
x_{g}	Grid
x_{i}	Input
x_{in}	Input of the inverter
x_{L}	Variable based on inductor
x_{o}	Output
x_{-o}	Open loop
x_{q}	Q-component
x_{s}	Source

Abbreviations

$\alpha\beta 0$	Stationary reference frame
AC	Alternating current
DC	Direct current
DFT	Discrete Fourier transformation
FFT	Fast Fourier transformation
IGBT	Insulated gate bi-polar transistor
I/O	Input-output
IV	Current-voltage
LHP	Left half plane
MLBS	Maximum-length binary sequence
MPP	Maximum power point
PHIL	Power-hardware-in-the-loop
PI	Proportional-integral controller
PLL	Phase-locked-loop
PV	Photovoltaic
PRBS	Pseudo-random binary sequence
PWM	Pulse-width modulation
RHP	Right half plane
SNR	Signal-to-noise ratio
SRF	Synchronous reference frame
XOR	Exclusive-or

1 Introduction

There have been significant changes in the energy field in recent years and the changes will continue in the future due to tightened environmental regulations and increases in the price of traditional fossil energy sources. Global energy trend will be based on the environmentally friendly renewable energy production and energy efficiency.

The most common way to connect renewable energy generators to the grid is through inverters. The main function of the inverter is to transform the power of the energy source to a suitable form for the power grid. Fig. 1 illustrates the basic idea of grid connection of a photovoltaic (PV) generator. The amount of grid-connected power electronic devices is increasing because of the demand of energy saving and fast growing distributed renewable energy production which requires power electronics inverters at the connection point with the grid. [1]

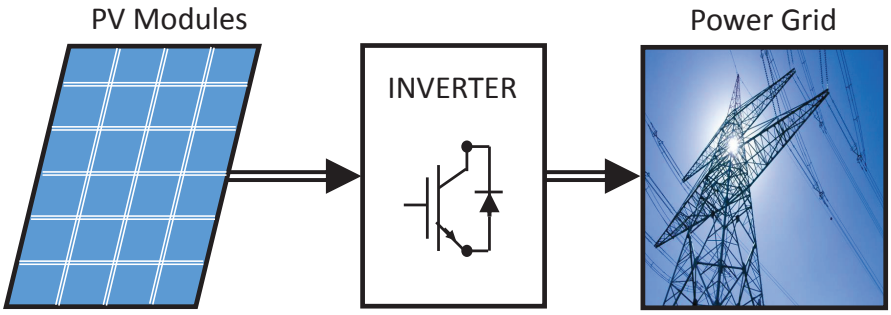

Figure 1: PV-generator is connected to the power grid through inverter.

Recent studies have shown that the increasing amount of new power electronics and distributed energy production will significantly affect the grid dynamics, power quality and even cause instability [2]. When considering the power electronic devices, time varying grid characteristics have the significant effect on the operation of the system. Grid can be introduced to the inverter as an impedance which varies over the time and thus describing effectively the grid conditions. Also the inverters can be analyzed using their output impedance seen from the grid side. One of the most studied power quality problem is harmonic resonance. Harmonic resonance between the grid and inverter can be seen as an impedance-mismatches at the interconnection point. [3] Thus, the grid impedance is one of the many design parameters that has to be considered when tuning the control system of the inverter. Therefore, accurate grid and inverter impedance information is essential for the control design of the grid-connected inverters and for stability analysis.

Since the grid impedance varies over time and with many parameters, the offline design for one specific operating point is insufficient when tuning the inverter control system. Hence, automatically changing control parameters based on the real-time grid-impedance measurement is most desirable. [4]

When the operating conditions vary over time, the inverter controller should adapt to different operating points [5]. One idea is to produce control system that adjusts the actual control system parameters of the inverter suitable for the current operating point, which is called adaptive control. When considering grid-connected devices the grid conditions define the operating point. Thus adaptive control of the grid-connected inverters is based on real-time grid impedance measurements and the control system reacts according to different grid conditions by changing the parameters of the control system. That requires accurate dynamic model of the actual inverter and real-time online grid impedance measurements in order to design the adaptive control properly.

In this thesis grid impedance is measured in the frequency domain by using non-parametric methods. Basic idea of the non-parametric measurements is that the system characteristics can be identified by using only the input and output signals [6]. Adaptive control of grid-connected systems requires real-time online measurements of the grid impedance. Hence, very fast frequency response measurement method is required to provide information about the grid impedance to the adaptive control system as close to real-time as possible. Broadband injection signals and Fourier techniques provide methods for fast frequency-response measurements. In these methods, a broadband signal is injected into a system, its response is collected and the transfer function is computed as a frequency response by using Fourier techniques. [7]

One of the most common broadband injections in the field of frequency-domain system identification is pseudo-random binary sequence (PRBS). It provides very fast measurements [8] and it has proven to be effective in numerous applications including frequency-domain analysis of switched-mode power supplies [9], grid-connected three-phase inverters [10] and grid impedance measurements [5]. The PRBS is easy to generate with the use of XOR-port and shift registers. Amplitude of the signal can be kept relatively small and thus the PRBS is suitable for sensitive systems in which the high amplitude of the perturbation signal would affect to the system behavior. In this thesis, the PRBS method is used to implement real-time grid-impedance measurements.

Simplified models of the real systems are often used by the control designers

because they want to focus more on the control problems. Those models contain lot of assumptions and approximations compared to the actual systems. Hence, it is important for control designer to prototype new control designs with actual hardware as soon as possible. This can be done with the use of power-hardware-in-the-loop (PHIL) tests where a real-time simulator such as dSPACE is used to implement the control system of actual hardware. [11] For years, the control system had to be tested by writing the code to microprocessors of the devices by hand. Now there are applications that automatically build a C-code of the simulation model and provide the interface to control the real device [12]. Those systems have reduced transferring time from the simulations to the PHIL tests.

This thesis will introduce an effective PHIL method that combines real-time online grid impedance measurement system and adaptive control of grid-connected inverters based on current grid impedance. The applied methods do not require any other measurement device, only the inverter and it's control system.

This thesis is divided into six main sections. After introduction the Section 2 introduces modeling of grid-connected inverters, control system of inverters and stability analysis to support understanding the rest of the thesis. Section 3 will introduce measurement methods applied in experiments of the thesis. Section 4 introduces the methods applied in adaptive control. Section 5 presents experimental tests supporting the theoretical findings and prove the functionality of applied methods. Section 6 will draw conclusions.

2 Impedance-Based Stability

The stability of grid-connected inverter at interconnection point with the grid can be considered as ratio between grid impedance and inverter impedance. The grid impedance varies over time and thus the real-time measurements of it are required for continuous stability analysis. Inverter impedance is affected by control design and can be calculated from accurate analytical model of the inverter.

2.1 Modeling of Grid-Connected Inverters

DQ-Domain

Three-phase systems are complex to identify by using directly three AC components (i.e. *abc*-domain). Three AC-components are sine waves at their fundamental frequency (e.g. 60 Hz) as Fig. 2 shows. The signals in *abc*-domain are thus time varying signals and also their steady-state value varies with time. Three-phase grid-connected systems are often linearized around their steady-state operating point in dynamic modeling. Hence, *abc*-domain is not very practical choice for dynamic modeling of three-phase systems.

DC-valued signals have time-invariant steady-state values and thus enables dynamic models of electrical systems to be linearized near the specific operating point. There are mathematical transformations where balanced three-phase signals can be transformed into two DC signals without losing any information. The domain in which three-phase system is determined by three DC signals is called the synchronous reference frame. Transformation from time varying three-phase signals to two time invariant signals can be done in two steps. In first step the stationary reference frame is presented using Clarke's transformation which transforms three-phase signals to a rotating vector [13]. Rotating vector has three-phase components alpha (α), beta (β) and zero (0) which is called as stationary reference frame. The amplitude invariant transformation can be written as [14]

$$\begin{bmatrix} x_\alpha(t) \\ x_\beta(t) \\ x_0(t) \end{bmatrix} = \frac{2}{3} \begin{bmatrix} 1 & -1/2 & -1/2 \\ 0 & \sqrt{3}/2 & -\sqrt{3}/2 \\ 1/2 & 1/2 & 1/2 \end{bmatrix} \begin{bmatrix} x_a(t) \\ x_b(t) \\ x_c(t) \end{bmatrix} \tag{1}$$

where $x_\alpha(t)$, $x_\beta(t)$ and $x_0(t)$ are signals in $\alpha\beta 0$-domain, $x_a(t)$, $x_b(t)$ and $x_c(t)$ are *acb*-domain signals and the matrix in the middle is called as Clarke's

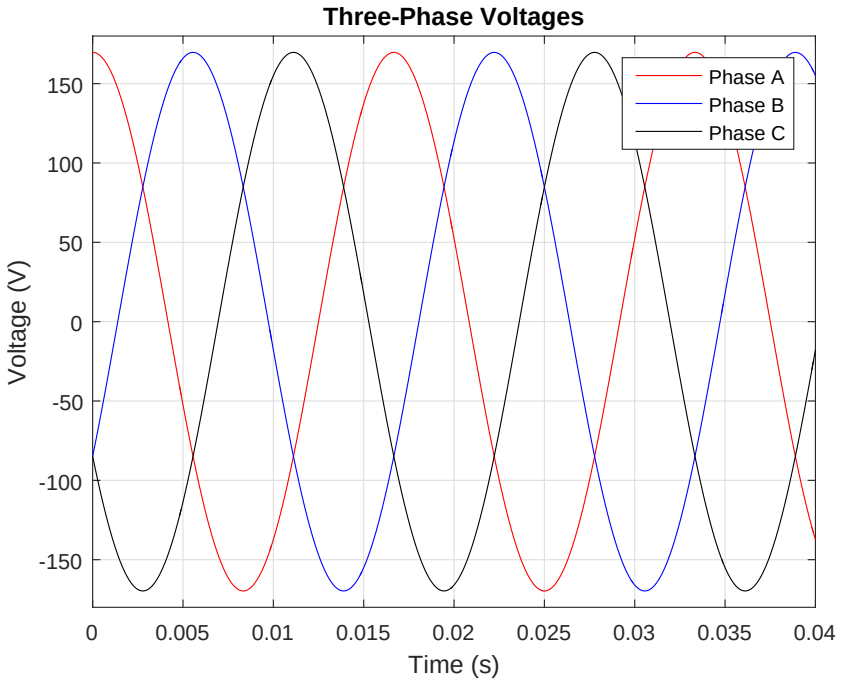

Figure 2: Three-phase voltages at the fundamental frequency of 60 Hz.

matrix. The Clarke's matrix has constant factor of $2/3$ because the amplitude invariant $\alpha\beta$-transformation is used. In balanced three-phase system the zero-component in stationary reference frame can be neglected as (1) implies and hence the three-phase signals can be presented as two AC-signals as Fig. 3 shows.

DC-valued steady-state operating point can not be defined in stationary reference frame because signals still have sinusoidal form. The sine wave is seen as rotating vector in stationary reference frame. The reference frame can also rotate. The reference frame that rotates at the same fundamental frequency (here 60 Hz) is called as synchronous reference frame because it is synchronized with the frequency of the phase voltages. In synchronous reference frame the rotating vector from the stationary reference frame is seen as stationary vector and hence the DC-valued steady-state operating point can be defined. This is called the dq-domain because it contains the DC-valued direct (d) and quadrature (q) -components [15]. There is basically also the zero component but it can be neglected in three-phase system as in $\alpha\beta 0$-domain. The effect of rotation of the reference to the signal can be written asf_{gen}

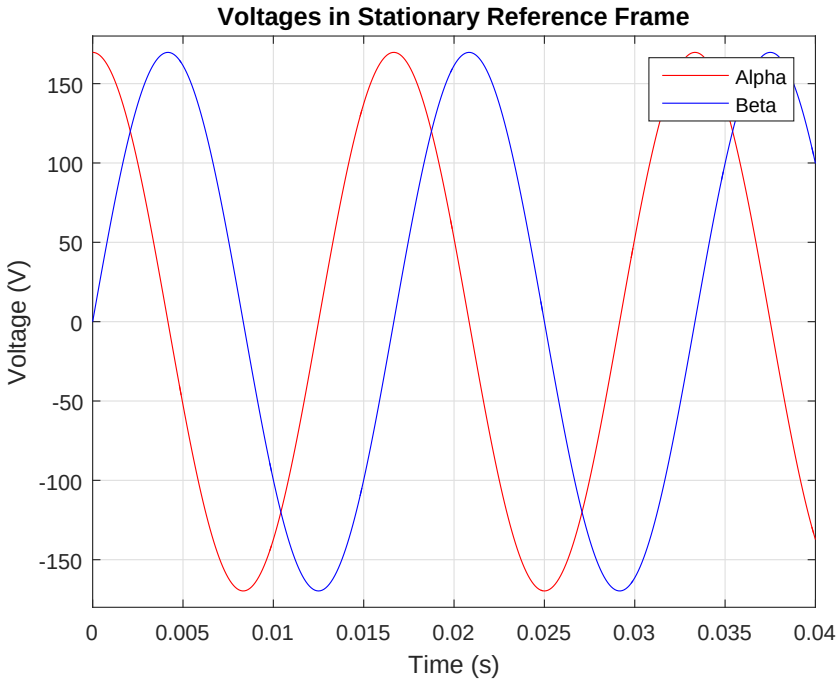

Figure 3: Three-phase voltages in the stationary reference frame.

$$\begin{bmatrix} x_d \\ x_q \\ x_0 \end{bmatrix} = \begin{bmatrix} \cos(\omega t) & \sin(\omega t) & 0 \\ \text{-}\sin(\omega t) & \cos(\omega t) & 0 \\ 0 & 0 & 1 \end{bmatrix} \begin{bmatrix} x_\alpha(t) \\ x_\beta(t) \\ x_0(t) \end{bmatrix} \tag{2}$$

where x_d, x_q and x_0 are signals in dq-domain, $x_\alpha(t)$, $x_\beta(t)$ and $x_0(t)$ are signals in $\alpha\beta 0$-domain, ω is the fundamental frequency and the matrix represents the rotation of the reference frame. It should be noted that signals in dq-domain are time-invariant. Hence, the DC-valued steady-state operating point can be defined in the dq-domain. In ideal and balanced three-phase system the d-component has the DC value that represents the amplitude of grid voltages and q-component is zero as Fig. 4 shows.

The Park's transformation is a combination of Clarke's transformation and the rotating reference frame. Park's transformation transforms three-phase signals directly to the synchronous reference frame and can be formed as

$$\begin{bmatrix} x_d \\ x_q \\ x_0 \end{bmatrix} = \begin{bmatrix} \cos(\omega t) & \sin(\omega t) & 0 \\ \text{-}\sin(\omega t) & \cos(\omega t) & 0 \\ 0 & 0 & 1 \end{bmatrix} \frac{2}{3} \begin{bmatrix} 1 & -1/2 & -1/2 \\ 0 & \sqrt{3}/2 & -\sqrt{3}/2 \\ 1/2 & 1/2 & 1/2 \end{bmatrix} \begin{bmatrix} x_a(t) \\ x_b(t) \\ x_c(t) \end{bmatrix} \tag{3}$$

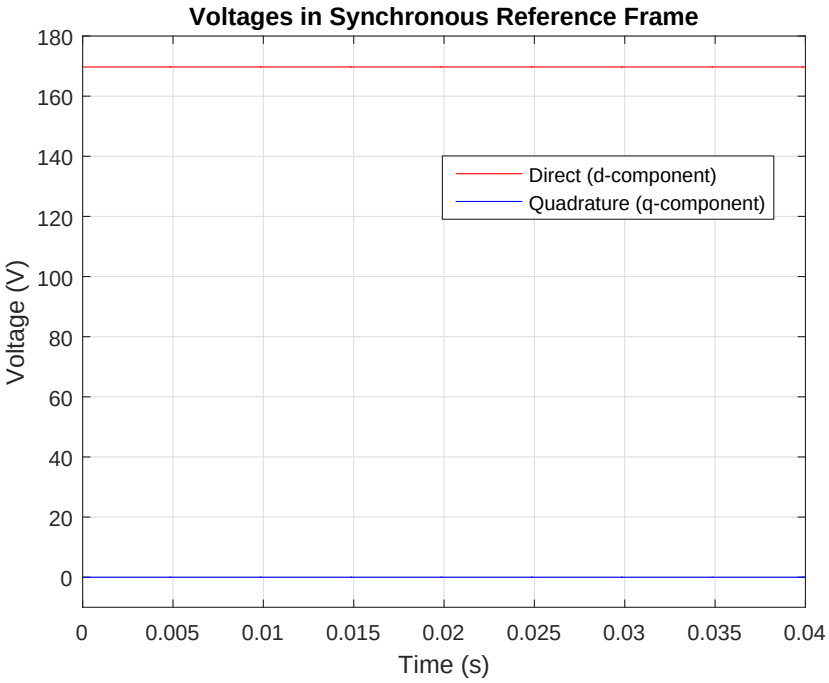

Figure 4: Three-phase voltages in the synchronous reference frame.

Conventional PI-controllers can regulate DC-valued error signals. Hence, the control of three-phase grid-connected inverters are often implemented in the *dq*-domain and PI-controllers are used.

In three-phase systems d- and q-components are coupled [16]. This is a drawback of using dq-domain but the cross-coupling can be compensated by using decoupling gains. In dq-domain the d- and q-components are in 90° phase shift i.e. the d-component can be considered to represent the positive real axis (x_d) and q-component the positive imaginary axis (jx_q) of the complex plane. Akagi et al. introduced the instantaneous power theory for *dq*-domain which defines the apparent power as [17]

$$\mathbf{s} = \mathbf{p} + j\mathbf{q} = \mathbf{v} \times \mathbf{i}^* = (v_d i_d + v_q i_q) + j(v_q i_d - v_d i_q). \tag{4}$$

In this thesis the inverter control system regulates the v_q to zero and thus the the real and reactive power can be simplified as

$$\mathbf{p} = v_d i_d \tag{5}$$

and

$$\mathbf{q} = -v_d i_q. \tag{6}$$

This introduces one of the main advantages of the *dq*- which is that the real and reactive powers can be controlled separately with the use of DC-valued currents i_d and i_q.

Small-Signal Model

Small-signal model allows the nonlinear device to be analyzed with the use of linear equations near the steady-state operating point [6]. Fig. 5 shows the power stage of a three-phase grid-connected inverter where the source is modeled by Norton equivalent current source and the load is modeled by Thevenin equivalent voltage source (sink). Inverter itself is modeled with three pairs of IGBT transistors as switches, pair for each phase.

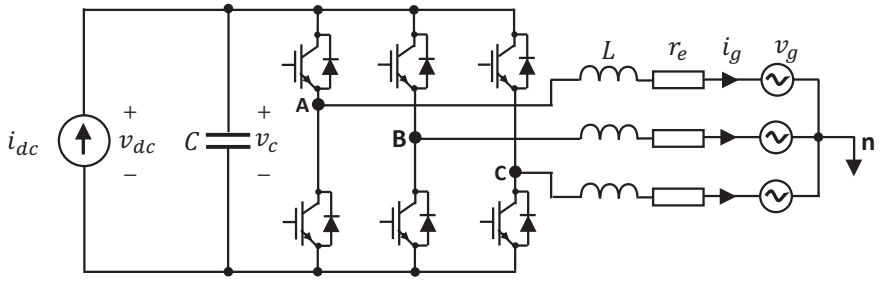

Figure 5: Three-phase inverter.

The average model of switching devices contains the averaged values over the one switching period. The values are weighted with the duty ratio d of the switches to illustrate the effect of on and off times. The average model of the inverter shown in Fig. 5 can be written as follows

$$\frac{d\langle i_{Ld}\rangle}{dt} = -\frac{r_e i_{Ld}}{L} + \omega_s i_{Lq} + \frac{d_d v_c}{L} - \frac{v_{od}}{L}, \tag{7}$$

$$\frac{d\langle i_{Lq}\rangle}{dt} = -\omega_s i_{Ld} - \frac{r_e i_{Lq}}{L} + \frac{d_q v_c}{L} - \frac{v_{oq}}{L}, \tag{8}$$

$$\frac{d\langle v_c\rangle}{dt} = -\frac{3}{2}\frac{i_{Ld}d_d}{C} - \frac{3}{2}\frac{i_{Lq}d_q}{C} + \frac{i_{in}}{C}, \tag{9}$$

$$\langle v_{in}\rangle = \langle v_c\rangle, \tag{10}$$

$$\langle i_{od}\rangle = \langle i_{Ld}\rangle, \langle i_{oq}\rangle = \langle i_{Lq}\rangle, \tag{11}$$

where r_e takes account the resistance of the switch and the phase inductor, C is the DC capacitor, L is the phase inductor and ω_s is the angular frequency of the fundamental grid voltage component. The voltages and currents of the three-phase inverter from Fig. 5 are transferred to the dq-domain as: i_{Ld} and i_{Lq} are the inductor currents, v_c is the DC capacitor voltage, i_{dc} is the DC current, v_{in} is the DC voltage and v_{od} and v_{oq} are the grid voltages. The inverter output currents i_{od} and i_{oq} are the same as inductor currents i_{Ld} and i_{Lq}. To simplify equations parasitic resistance of the DC capacitor is neglected thus the input voltage and capacitors voltage is the same. Three-phase duty ratios d_{abc} are presented in dq-domain as d_d and d_q. According to basic circuit theory the d and q-components couple to each other via inductor current because the impedance of ideal inductor is $Z_L = j\omega L$ where L is the inductance value. When voltages are kept constant the inductor lags currents -90°($= -j$) and it is also known that $j^2 = -1$. Hence, the inductor current d-component couples to inductor voltage q-component as

$$v_{Lq-coupling} = L\frac{d(i_{Lq-coupling})}{dt} = i_{Ld}(-j\omega_s L) = -j(i_{Ld}\omega_s L), \tag{12}$$

and inductor current q-component couples to inductor voltage d-component as

$$v_{Ld-coupling} = L\frac{d(i_{Ld-coupling})}{dt} = ji_{Lq}(-j\omega_s)L = -j^2(i_{Lq}\omega_s L) = i_{Lq}\omega_s L, \tag{13}$$

where ω_s is the fundamental frequency of the system.

Next the steady-state operating point is calculated by setting the derivatives equal to zero and denoting all the variables as steady-state values (capital letters). The q-components of currents and voltages can be neglected because

they are close to zero when inverter is operating properly. Thus (7) - (9) can be rewritten as

$$0 = -\frac{3}{2}\frac{I_{Ld}D_d}{C} + \frac{I_{in}}{C}, \tag{14}$$

$$0 = -\frac{r_e I_{Ld}}{L} + \frac{D_d V_c}{L} - \frac{V_{od}}{L}, \tag{15}$$

$$0 = -\omega_s I_{Ld} + \frac{D_q V_c}{L}. \tag{16}$$

The steady-state values of the variables can be solved from (14) - (16). The values of I_{in} and V_c $(= V_{in})$ are determined from source and V_{od} is determined from the grid voltage. The steady-state values are

$$D_d = \frac{V_{od} + \sqrt{{V_{od}}^2 + \frac{8}{3}V_{in}r_e I_{in}}}{2V_{in}}, \tag{17}$$

$$D_q = \frac{2I_{in}L\omega_s}{3D_d V_{in}}, \tag{18}$$

$$I_{Ld} = \frac{2I_{in}}{3D_d}. \tag{19}$$

The average model is linearized by using first-order partial derivatives of each input and state variable. Partial derivatives are taken to illustrate on how their small changes affects to other variables. The linearized model close to the steady-state operating point of the inverter can be defined as

$$\frac{d\hat{i}_{Ld}}{dt} = -\frac{r_e}{L}\hat{i}_{Ld} + \omega_s\hat{i}_{Lq} + \frac{D_d}{L}\hat{v}_c - \frac{1}{L}\hat{v}_{od} + \frac{V_c}{L}\hat{d}_d, \tag{20}$$

$$\frac{d\hat{i}_{Lq}}{dt} = -\omega_s\hat{i}_{Ld} - \frac{r_e}{L}\hat{i}_{Lq} + \frac{D_q}{L}\hat{v}_c - \frac{1}{L}\hat{v}_{oq} + \frac{V_c}{L}\hat{d}_q, \tag{21}$$

$$\frac{d\hat{v}_c}{dt} = -\frac{3}{2}\frac{D_d}{C}\hat{i}_{Ld} - \frac{3}{2}\frac{D_q}{C}\hat{i}_{Lq} + \frac{1}{C}\hat{i}_{in} - \frac{3}{2}\frac{I_{Ld}}{C}\hat{d}_d - \frac{3}{2}\frac{I_{Lq}}{C}\hat{d}_q, \tag{22}$$

$$\hat{v}_{in} = \hat{v}_c, \tag{23}$$

$$\hat{i}_{od} = \hat{i}_{Ld}, \hat{i}_{oq} = \hat{i}_{Lq}, \tag{24}$$

where '$\hat{}$' denotes the partial derivative of the variable. When input, output and state variables are collected in their own groups as vectors and constants in matrix, the linearized model can be shown as matrix form as

$$\frac{d\mathbf{x}}{dt} = \begin{bmatrix} 0 & -\frac{3}{2}\frac{D_d}{C} & -\frac{3}{2}\frac{D_q}{C} \\ \frac{D_d}{L} & -\frac{r_e}{L} & \omega_s \\ \frac{D_q}{L} & -\omega_s & -\frac{r_e}{L} \end{bmatrix} \mathbf{x} + \begin{bmatrix} \frac{1}{C} & 0 & 0 & -\frac{I_{dc}}{CD_d} & 0 \\ 0 & -\frac{1}{L} & 0 & \frac{V_c}{L} & 0 \\ 0 & 0 & -\frac{1}{L} & 0 & \frac{V_i n}{L} \end{bmatrix} \mathbf{u} \tag{25}$$

$$\mathbf{y} = \begin{bmatrix} 1 & 0 & 0 \\ 0 & 1 & 0 \\ 0 & 0 & 1 \end{bmatrix} \mathbf{x} + \mathbf{0u} \tag{26}$$

where the small signal input and output signal vectors are defined as

$$\mathbf{x} = \begin{bmatrix} \hat{i}_{Ld} \\ \hat{i}_{Lq} \\ \hat{v}_c \end{bmatrix}, \mathbf{u} = \begin{bmatrix} \hat{i}_{in} \\ \hat{v}_{od} \\ \hat{v}_{oq} \\ \hat{d}_d \\ \hat{d}_q \end{bmatrix}, \mathbf{y} = \begin{bmatrix} \hat{i}_{od} \\ \hat{i}_{oq} \\ \hat{v}_{in} \end{bmatrix} \tag{27}$$

The matrix form can be transformed to the frequency-domain using Laplace transform as

$$s\mathbf{x} = \mathbf{A}\mathbf{x} + \mathbf{B}\mathbf{u} \tag{28}$$

$$s\mathbf{y} = \mathbf{C}\mathbf{x} + \mathbf{0}\mathbf{u} \tag{29}$$

where state matrix $\mathbf{A}$ is the first matrix and $\mathbf{B}$ is the second matrix in (25) and $\mathbf{C}$ is the matrix in (26). The transfer matrix $\mathbf{G}$ from the inverter input to output can be solved with the use of equation [18]

$$\mathbf{Y}(s) = \mathbf{G}\mathbf{U}(s) = \left[\mathbf{C}(s\mathbf{I} - \mathbf{A})^{-1}\mathbf{B}\right]\mathbf{U}(s) \tag{30}$$

where $\mathbf{I}$ is identity matrix. In this case (30) yields the input-to-output transfer function $\mathbf{G}$ which includes 15 different open-loop transfer functions from which the dynamics of the inverter can be solved. The resulting transfer matrix from input to output can be presented as

$$\begin{bmatrix} \hat{i}_{od} \\ \hat{i}_{oq} \\ \hat{v}_{in} \end{bmatrix} = \begin{bmatrix} A_{iod-o} & -Y_{d-o} & -Y_{dq-o} & G_{cod-o} & G_{codq-o} \\ A_{ioq-o} & -Y_{qd-o} & -Y_{q-o} & G_{coqd-o} & G_{coq-o} \\ Z_{in-o} & T_{iod-o} & T_{ioq-o} & G_{cid-o} & G_{ciq-o} \end{bmatrix} \begin{bmatrix} \hat{i}_{in} \\ \hat{v}_{od} \\ \hat{v}_{oq} \\ \hat{d}_d \\ \hat{d}_q \end{bmatrix} \tag{31}$$

where Z denotes impedance, Y admittance, T is voltage-to-voltage transfer function (transmittance), A is current-to-current transfer function and G is transfer function that represents the effect of the duty ratio. Admittances have negative sign because the output current flowing toward the converter is defined positive. The lower index '$-o$' denotes the open-loop dynamics, 'i' DC side, 'o' AC side, 'c' control, 'd' d component, 'q' q component and 'dq' ('qd') cross coupling component.

2.2 Control System of Grid-Connected Inverter

Three-phase inverters are often analyzed in dq-domain because PI-controllers can handle only DC-valued error signals [19]. Fig. 6 illustrates simplified control system of the inverter. Pulse width modulator (PWM) block produces the switching signals for every phase based on the calculated duty ratios d_{abc}

of the outer control system. Phase-locked-loop (PLL) synchronizes the phase of the inverter output current with the grid. The estimated phase is required by dq-transformation. Duty ratios are output of the current control block which regulates the inverter output currents according to the reference value. The reference signal in PV-inverters is calculated in DC-voltage control in order to reach suitable operating point of the PV-generator. The maximum power point (MPP) of the PV-generator is determined by the DC voltage which affect the output currents. Hence, the reference signal for DC-voltage control is set in order to reach PV-generators MPP. It is important to notice that all of the control of inverter is basically based on the modification of duty ratios d_d and d_q of the inverter switches.

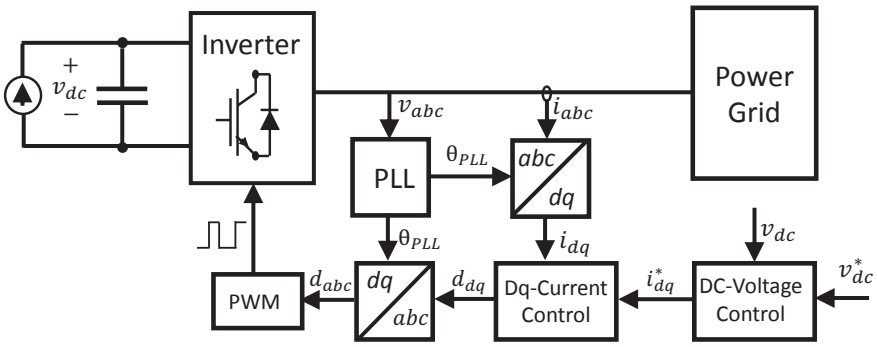

Figure 6: Simplified inverter control system.

Cascaded control system is used as control strategy in this thesis. DC-voltage control acts as an outer control loop and current control as an inner control loop. In cascaded control system the inner control loop should be faster than outer control loop because the inner loop has to react to changes of its reference provided by outer loop. Faster control loop means in practice that the cross-over frequency is higher. Different closed loop control systems can be identified separately and then processed as open loop transfer functions. [20] Next subsections will introduce control methods that are commonly used to synchronize the inverter to the grid.

PI-controller

PI-controller includes proportional and integral terms. The PI-controller is basically a feedback system that regulates the error signal between the measured variable and the reference. Proportional term processes the present

error by adjusting control signal to be large if the error signal is large. Integral term processes also the past error to eliminate steady-state error. The PI-controller can process only DC-valued signals and hence it is implemented in the dq-domain. The transfer function of the PI-controller can be written as [21]

$$G_{\mathrm{PI}} = K_p + \frac{K_i}{s} = \frac{K_p s + K_i}{s}, \tag{32}$$

where K_p is the gain of the proportional term and K_i is the gain of the integral term. The PI-controller can be tuned by adjusting the gains [22]. In this thesis PI-controllers are tuned with the use of loop shaping technique such that the current control loop has sufficient bandwidth and phase margins. Loop shaping technique is presented further in section 3.3. Fig. 7 shows a block diagram of the simple system that regulates the output value of the process to its reference value with the use of feedback loop and a PI-controller.

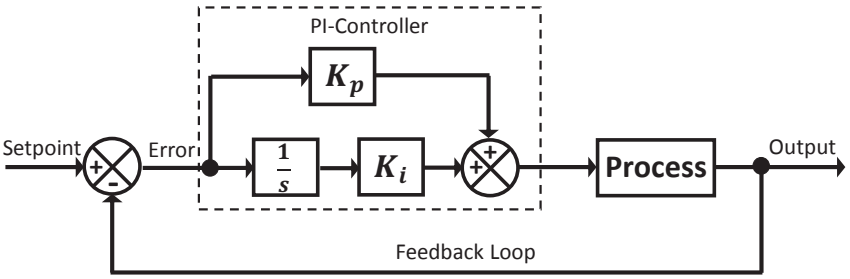

Figure 7: Block diagram of the conventional PI-controller with process itself and a feedback loop.

Phase-Locked-Loop

The inverter control system synchronizes the inverter output current with phase and frequency of the grid voltage with the use of phase-locked-loop (PLL). PLL estimates the phase of the grid voltages. The phase angle is fed to dq-transformations and q-component current controller of the inverter which modifies duty ratio d_q when cross-couplings are neglected. Hence, the PLL synchronizes the inverter output current with the grid voltage via current controllers to maximize the active power flow from inverter to the grid. One of the best known grid synchronizing techniques is synchronous

reference frame PLL (SRF-PLL). It transforms the grid voltages from *abc*-domain to the *dq*-domain with the use of Park's transformation. SRF-PLL applies *dq*-domain grid voltages to estimate the phase angle and frequency of the grid and then the current control regulates the sensed output current q-component to zero in normal case when only real power is desired [14]. Simplified block diagram of the conventional SRF-PLL can be seen in Fig. 8 which estimates phase angle of the grid voltages.

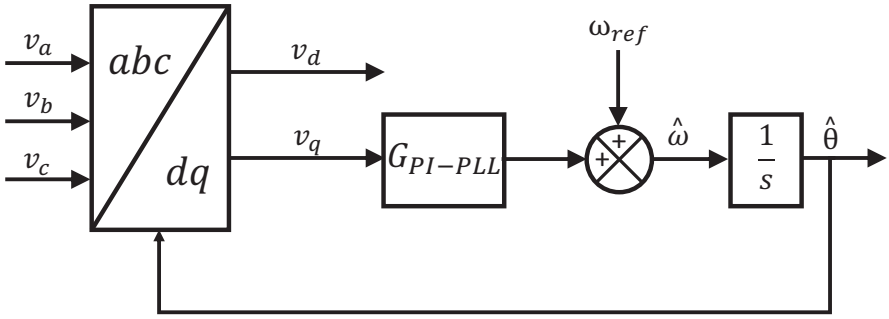

Figure 8: Simplified control diagram of the conventional SRF-PLL.

The SRF-PLL shown in Fig. 8 has the three-phase grid voltages v_{abc} as input variables. Three-phase grid voltages are transformed to the synchronous reference frame with the use of *dq*-transformation. The linearized model of the SRF-PLL at certain steady-state operating point has to be derived when including the SRF-PLL model to the closed-loop inverter model. Fig. 9 shows the small-signal block diagram of the linearized SRF-PLL. PI-controller derives the frequency difference $\hat{\omega}$ from error between sensed grid voltage q-component $\hat{v}'_{oq}$ and its reference $\hat{v}^*_{oq}$. Reference value for the voltage q-component is set to zero to achieve ideal grid synchronization. By integrating frequency error, the phase angle difference $\hat{\theta}$ is finally developed as output of the SRF-PLL.

When considering the linearized model of SRF-PLL the sensed values for d and q-components can be written as [23]

$$\hat{x}'_d = \hat{x}_d + \Theta_\Delta \hat{x}_q + X_q \hat{\theta} \tag{33}$$

$$\hat{x}'_q = \hat{x}_q - \Theta_\Delta \hat{x}_d - X_d \hat{\theta}, \tag{34}$$

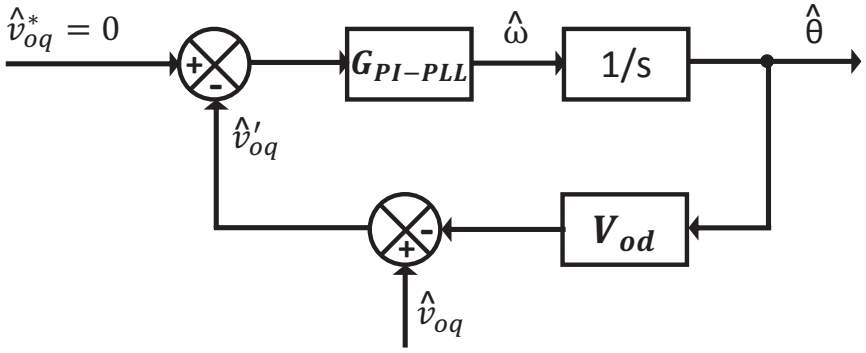

Figure 9: Block diagram of the small-signal model of the conventional SRF-PLL.

which shows the connections between the d and q-components. Θ_{Δ} is the steady-state of the phase difference which is zero in ideal grid synchronization. The sensed voltage q-component can be thus written as

$$\hat{v}_{oq}^{'} = \hat{v}_{oq} - V_d\hat{\theta}. \tag{35}$$

When it is assumed that $\hat{v}_{oq}^{*} = 0$ in Fig. 9, the loop gain for PLL is introduced as

$$L_{PLL} = \left(-\frac{V_{od}}{s}\right) G_{PI-PLL}. \tag{36}$$

With the loop gain the closed loop transfer function of the conventional SRF-PLL with PI-controller is simplified as

$$G_{\mathrm{PLL}} = \frac{1}{V_{od}} \left(\frac{L_{PLL}}{(1 + L_{PLL})}\right), \tag{37}$$

which can be controlled by adjusting gains of the PI-controller as presented.

By using the closed loop transfer function the phase angle difference is derived as

$$\hat{\theta} = \frac{1}{V_{od}} \left(\frac{L_{PLL}}{(1 + L_{PLL})}\right) \hat{v}_{oq}, \tag{38}$$

which is the output variable of the SRF-PLL.

Applied PI-controller affects on dynamics of the SRF-PLL. Bandwidth of the system transfer function defines how high frequencies it passes through. Bandwidth of the SRF-PLL (ω_{PLL}) should be high enough to allow fast dynamic responses in changing conditions. However, high bandwidth can cause instability under weak grid conditions by affecting on the inverter output impedance, and therefore, causing harmonic resonance in the connection point with the power grid (i.e. impedance-based instability). The bandwidth can be controlled by changing PI-controllers gains K_p and K_i [24]. Gains are chosen with the use of loop-shaping technique (discussed in section 3.3) to have required crossover frequency to the PLL loop gain.

DC-Voltage Control

It is assumed that only the d-components of currents affect the DC side of the inverter because DC side contains real power only. Hence, the DC-voltage controller is a PI-controller which have an error between sensed DC voltage v_{in} and its reference value v_{in}^* as an input. In PV-systems v_{in}^* is usually set to the MPP of the PV-generator. As output the DC-voltage controller have the reference value to the grid current d-component i_{od}^* which also affects on the DC voltage itself via current control loop. The DC-voltage control loop acts as an outer control loop and thus crossover frequency should be lower than in inner control loop. Also the harmonics that inverter produces can be attenuated by decreasing the crossover frequency of the DC-voltage controller. The DC voltage controller is denoted as G_{PI-dc} and the output of the controller can be written as

$$i_{od}^* = G_{PI-dc}(v_{in}^* - v_{in}). \tag{39}$$

Current Control Loop

Current control loop controls the output current of the inverter by changing duty ratios d_d and d_q of the switches. The control scheme is implemented with PI-controller which processes the error between reference output current and measured output current as an input. The transfer function of the current control loop is denoted as G_{PI}. In case of current-fed inverters with large DC capacitor the dynamics of the of the output current d and q-components have the same shape and thus the similar controllers can be used to control

both components. The reference value for the d-component (i^*_{od}) is provided by DC-voltage controller as (39) and the reference value for the q-component (i^*_{oq}) is set to zero to obtain unity power factor. Thus, the control laws of the current controllers can be defined as

$$d_d = G_{PI}(i^*_{od} - i_{od}) = G_{PI}(G_{PI-dc}(v^*_{in} - v_{in}) - i_{od}). \tag{40}$$

$$d_q = G_{PI}(0 - i_{od}). \tag{41}$$

LCL-Filter

Basically the LCL-filter is low-pass filter that reduces the higher order harmonics caused by switching. The filter contains capacitor C_f and the resistance of the damping resistance as R_{cf}. The inductance of the filter L_f is considered as a first inductor and grid-side inductance L_g (including the inductance of isolation transformer L_t) is considered as a second inductor of the LCL-filter. The inductance of the transformer and grid inductance L_g can not be changed. Thus the design parameters are the filter capacitance C_f and inductance L_f. The transfer function of LCL-filter can be written as [25]

$$H_{\text{LCL}} = \frac{1}{(L_g C_f L_f)s^3 + (L_g + L_f)s} \tag{42}$$

which can be modified easily by adjusting the capacitor value C_f. Greater value of C_f indicates the resonance peak of the LCL-filter to appear at the lower frequency and thus it filters more the higher frequencies. Eq. (42) also shows that the greater inductance values of L_g and L_f attenuate more the higher harmonics.

2.3 Impedance-Based Stability Analysis

Harmonic resonance (electromagnetic oscillation) is one of the most considered power quality problem. It causes power losses and even instability of the system. Harmonic resonance occurs in the grid current when the inverter operating does not match to the grid condition. The grid can be modeled as the grid impedance Z_L and the inverter as its output impedance Z_s. The

resonance occurs at the certain resonating frequency f_r (and its higher harmonics). At f_r the impedances cancel out imaginary parts (reactive power) of each other. Hence, at resonating frequency all of the stored energy transforms from energy of the magnetic field (inductor energy) to the electrical field energy (capacitor energy), two times in one period of f_r. This can be seen at the frequency where impedances have 180° phase difference. [26] The resonating effect can cause instability if the system magnifies the current at that frequency because then the resonance power is magnified at every period.

This thesis considers the stability analysis of the grid-connected systems which is based on the ratio of the grid impedance to the output impedance of the system under study. The impedance-based analyzes have shown to be effective in the stability analyzes and control of grid-connected devices as shown in [4] and [27].

Fig. 10 shows equivalent circuit of the source-load subsystem in which the source represents the inverter and load the power grid. Source (inverter) is modeled with Norton equivalent as current source with parallel impedance. Load (grid) is modeled with Thevenin equivalent as voltage sink and series impedance.

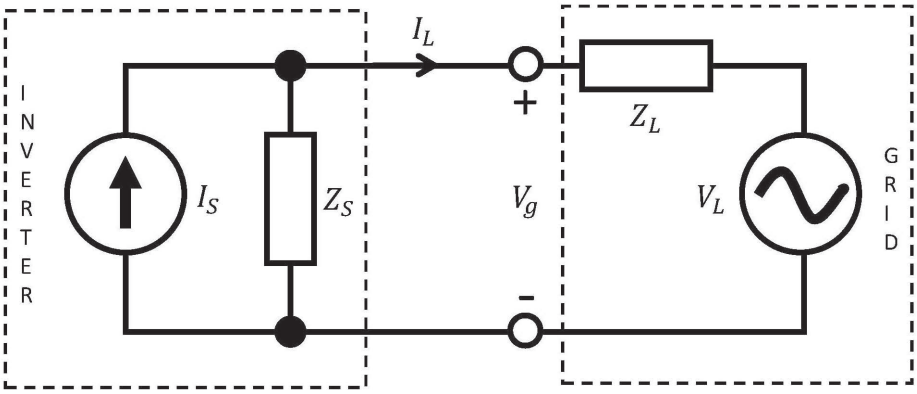

Figure 10: Source-load subsystem.

The stability is considered by determining if current from source to load (I_L) is stable. The current I_L in equivalent model represents the current flow between the inverter and the grid. The current can be written by applying Thevenin and Norton theorems as [4]

$$I_L = \frac{I_s Z_s}{Z_L + Z_S} - \frac{V_L}{Z_L + Z_S} = (I_s - \frac{V_L}{Z_S}) * \frac{1}{1 + \frac{Z_L}{Z_S}} \tag{43}$$

where the inverter output impedance is represented as a source impedance Z_S, the grid impedance is represented as a load impedance Z_L, I_s represents current of the source modeled as Norton equivalent current source and V_L represents load voltage as Thevenin equivalent voltage source. It is assumed that the inverter output impedance model is accurate and and the grid impedance is measured from actual grid. It is also assumed that the grid itself is stable and the inverter is designed to be stable when it is not connected [4]. Hence, it is assumed that I_s and $\frac{V_L}{Z_S}$ are stable. With these assumptions the stability analysis can be based on the characteristic polynomial of the system shown in Fig. 10 which can be written as [24]

$$p(s) = \frac{1}{1 + \frac{Z_L}{Z_S}}. \tag{44}$$

The interface between the grid and the inverter is stable if (46) satisfies the Nyquist stability criterion. The criterion states that system is stable if the Nyquist curve does not encircle clockwise the critical point (-1,0) in the complex-plane as shown in Fig. 11. [18] Fig. 11 shows that the system is marginally stable if the curve passes over the critical point.

The same stability analysis can be made by analyzing impedances in the frequency-domain as shown in Fig. 12 as a Bode-plot. The phase curve is the same for all presented curves and thus only one is shown in figure. The system is stable if the phase angle at the crossover (magnitude is 0 dB) frequency is higher than -180 degrees, i.e. there is a positive phase margin.

In the impedance-based stability analysis the phase angle and magnitude of the studied system is the phase and magnitude difference between the inverter and grid. Hence, if the phase difference between Z_S and Z_L at the frequency where impedances overlap in magnitude is more than 180 degrees, the system is unstable. Idea of determining the phase difference is illustrated in Fig. 13. The black line in the magnitude figure indicates the frequency where impedances overlap. The phase shift at the same frequency is illustrated with black arrow.

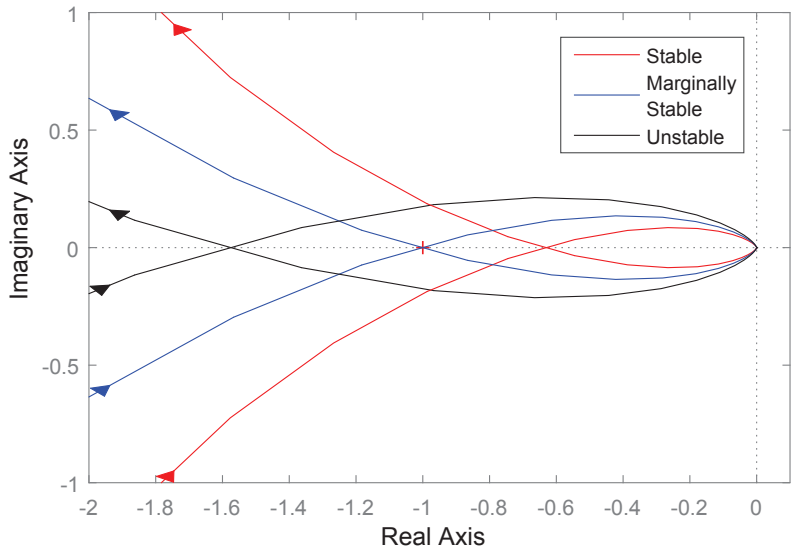

Figure 11: Nyquist curves of stable (red), marginally stable (blue) and unstable (black) systems.

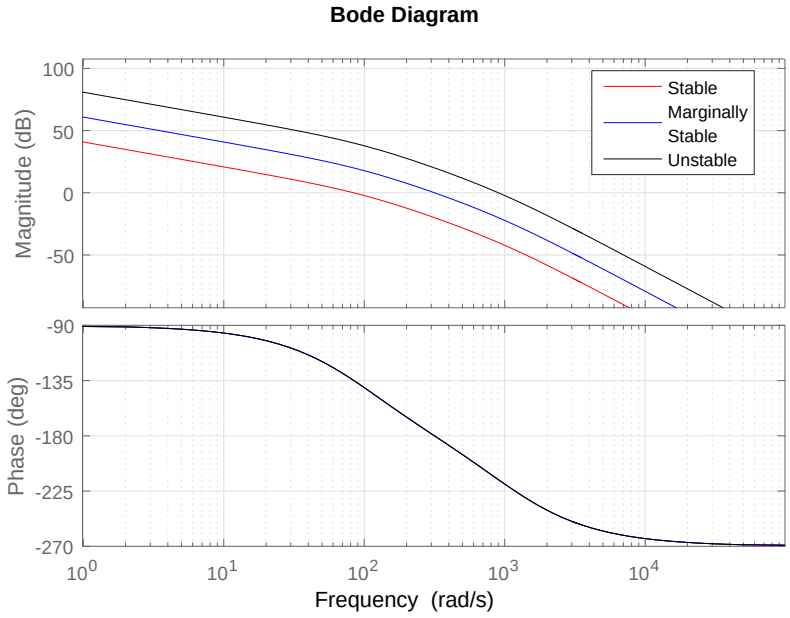

Figure 12: Bode plots of stable (red), marginally stable (blue) and unstable (black) systems.

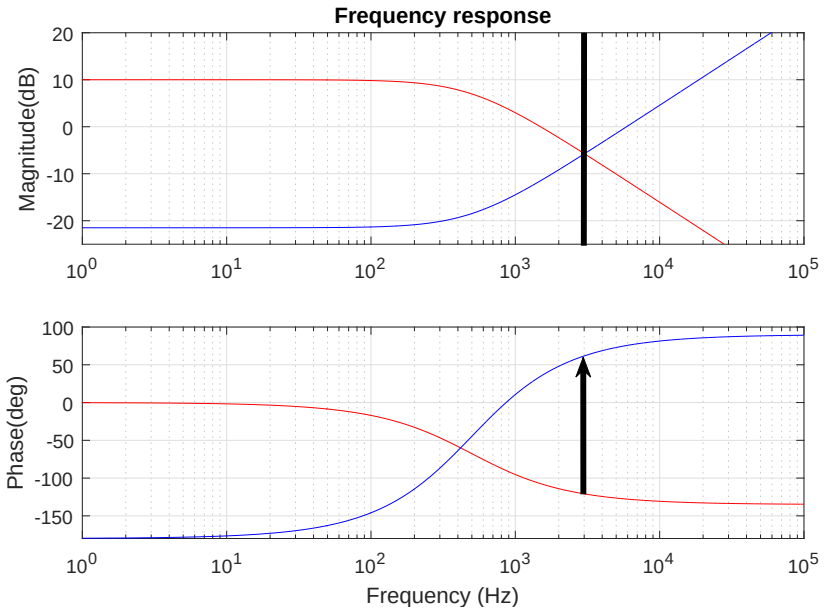

Figure 13: Bode plots of two systems and their phase difference (black arrow) at the frequency where impedances overlap in magnitude.

Impedance Mismatches and Impedance-Based Interactions

Weak grid can be understood as a very inductive element in low frequencies which phase increases to 90 degrees. In Fig. 5 the grid impedance is modeled only with inductance L_g and small resistance r_e. The basic inverter can be understood as a capacitive device with active components that decreases the phase under -90 degrees. Especially inverter output impedance q-component introduces negative resistance like behavior where phase angle stays -180 degrees below the crossover of the PLL. This is one of the possible reasons for the harmonic resonance between the grid and the grid-connected inverters. The harmonic resonance effect can be simplified by considering basic RLC resonance circuit which is known to resonate in certain frequency defined by values of L, R and C. When the parasitic resistance is neglected the electrical resonance effect occurs at the certain resonating frequency ω_r (equal to $2\pi f_r$) where

$$\omega_r L = \frac{1}{\omega_r C} \tag{45}$$

and thus

$$\omega_r = \frac{1}{\sqrt{LC}}. \tag{46}$$

In resonance the reactive power is transformed from electric field energy to the magnetic field energy twice at the period of the ω_r. [26] When considering the grid connected inverters, the resonance reduces the amount of real power and can cause even instability of the grid current when resonance is not damped and active components of the inverter is included. There is a possibility in the grid connected systems that the resonance at the frequency ω_r is magnified at every period and thus the system becomes unstable. That is called as undamped resonance and can lead to instability.

2.4 Inverter Output Impedance

Inverter output impedance can be represented by a transfer function from output current to output voltage. The output impedance must be solved separately for *d*- and *q*-components for the impedance-based stability analysis because they have different dynamics especially with the grid synchronization and DC-voltage controller.

Impedance d-Component

At the steady-state the amount of injected real power is much larger than reactive power. Thus, q-components does not affect much to the input dynamics. [28] Hence, it is assumed that only *d*-components affect to the input dynamics. Fig. 14 shows block diagram of the d-component open loop transfer functions with current control loop. This can be considered as output dynamics of the inverter d-component. The subscript '$-o$' denotes that the transfer function represents open loop dynamics. The current control loop gain can be defined as

$$L_{out-d} = G_{PI} G_{cod-o} \tag{47}$$

when the sensor gains and PWM modulator gain are assumed unity.

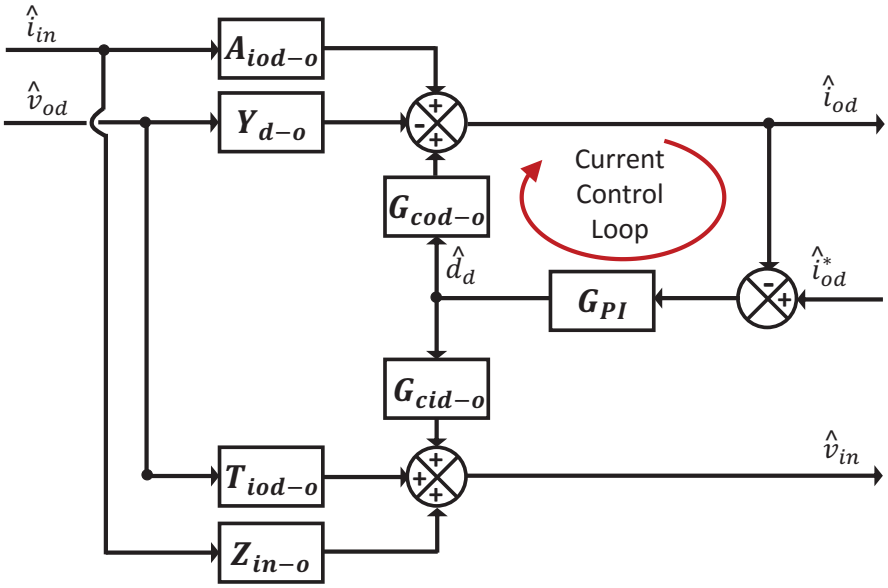

Figure 14: Block diagram of the d-component open loop transfer functions of the inverter with current control loop.

Closed loop transfer functions can be derived from Fig. 14. Closed loop transfer functions include the dynamics of the current control loop. They can be written as

$$A_{iod-cl} = \frac{\hat{i}_{od}}{\hat{i}_{in}} = \frac{A_{iod-o}}{(1 + L_{out-d})}, \tag{48}$$

$$G_{cod-cl} = \frac{\hat{i}_{od}}{\hat{i}^*_{od}} = \frac{L_{out-d}}{(1 + L_{out-d})}, \tag{49}$$

$$Y_{d-cl} = -\frac{\hat{i}_{od}}{\hat{v}_{od}} = \frac{Y_{d-o}}{(1 + L_{out-d})}, \tag{50}$$

$$Z_{in-cl} = \frac{\hat{v}_{dc}}{\hat{i}_{in}} = \frac{Z_{in-o}}{(1 + L_{out-d})} + \left(\frac{L_{out-d}}{(1 + L_{out-d})}\right)\left(Z_{in-o} - \frac{G_{cid-o}A_{iod-d}}{G_{cod-o}}\right), \tag{51}$$

$$G_{cid-cl} = \frac{\hat{v}_{in}}{\hat{i}^*_{od}} = \frac{G_{cid-o}}{G_{cod-o}}\left(\frac{L_{out-d}}{(1 + L_{out-d})}\right), \tag{52}$$

$$T_{oid-cl} = \frac{\hat{v}_{in}}{\hat{v}_{od}} = \frac{T_{oid-o}}{(1+L_{out-d})} + \left(\frac{L_{out-d}}{(1+L_{out-d})}\right)\left(T_{oid-o} + \frac{G_{cid-o}Y_{do}}{G_{cod-o}}\right) \quad (53)$$

where subscript '$-cl$' denotes the closed loop transfer function. Because of the cascaded control system of d-component the DC-voltage control can be added to the block diagram with closed loop transfer functions including current control. The derived closed loop transfer functions (including effect of the current control) can be handled as open loop transfer functions when DC-voltage control is investigated. The block diagram of the inverter with DC-voltage control is shown in Fig. 15 and can be seen as input dynamics of the inverter d-component.

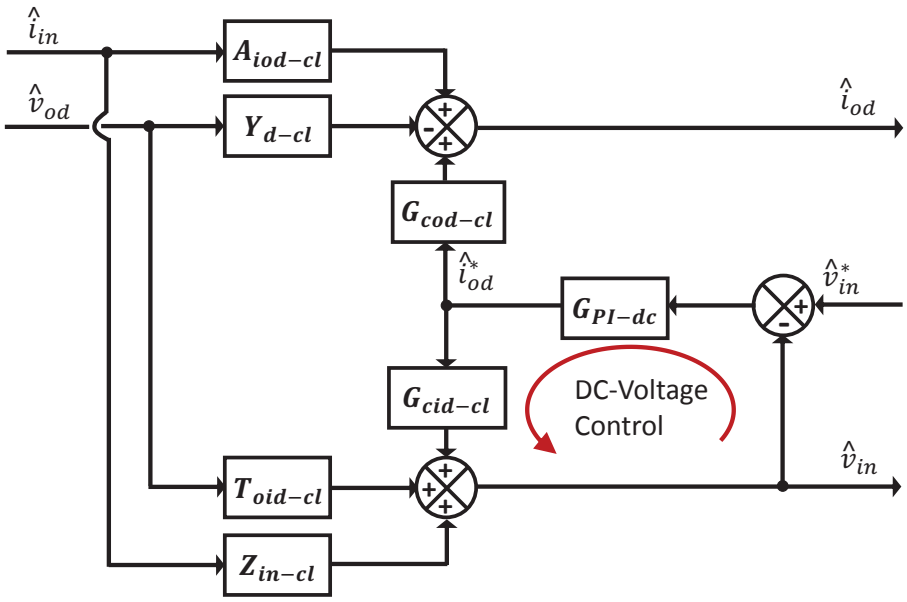

Figure 15: Block diagram of the inverter d-component with closed loop transfer functions and DC-voltage control.

The output impedance of the inverter is considered in this thesis and hence only it is presented when the DC-voltage control is added to closed loop dynamics. The DC-voltage control loop gain is considered as closed loop of the input dynamics by substituting G_{cid-cl} and approximating the sensor gains to be unity as

$$L_{in} = -G_{PI-dc}G_{cid-cl} = -\frac{G_{cid-o}}{G_{cod-o}}\left(\frac{L_{out-d}}{(1+L_{out-d})}\right)G_{PI-dc}, \quad (54)$$

The d-component of the inverter output admittance Y_{out-d} is the transfer function from the output voltage $\hat{v}_{od}$ to output current $\hat{i}_{od}$. Hence, the admittance can be derived from the Fig. 15 as

$$Y_{out-d} = -\frac{\hat{i}_{od}}{\hat{v}_{od}} = Y_{d-cl} + \frac{T_{oid-cl} G_{PI-dc} G_{cod-cl}}{(1 + L_{in})}. \tag{55}$$

The closed loop transfer functions from (48) - (53) are substituted and the transfer function is simplified as

$$Y_{out-d} = \frac{Y_{d-o}}{(1 + L_{in})(1 + L_{out-d})} + \left(\frac{L_{in}}{1 + L_{in}}\right)\left(Y_{d-o} + \frac{G_{cod-o} T_{oid-o}}{(1 + G_{cid-o})}\right) \tag{56}$$

from which the effect of current control loop gain (L_{out-d}) and DC-voltage control loop gain (L_{in}) to the output impedance can be seen.

Often the capacitor is added parallel to conduct high order harmonic currents to the ground. By adding the capacitor parallel with the AC-side inductance the LCL-filter is implemented. The admittance of the capacitor C_f can be calculated as

$$Y_c = \frac{C_f s}{(1 + R_{Cf} C_f s)}, \tag{57}$$

where R_{Cf} is the resistance of the capacitor. The capacitor admittance is taken account by adding it to the inverter output impedance. As an result the analytical output admittance of the grid connected inverter is derived. That can be written as

$$Y_{s-d} = Y_{out-d} + Y_C, \tag{58}$$

from which the output impedance of the inverter d-component can be calculated as $Z_{s-d} = 1/Y_{s-d}$ which is also considered as source impedance.

Impedance q-Component

Q-component control system is not assumed to have an effect on the input dynamics. Hence, effect of the q-component on the DC-voltage control can be neglected. As considered in section 2.2 the PLL affects on the q-component of the inverter output. The SRF-PLL products the phase error $\hat{\theta}$ compared to grid voltages as output and current control regulates the q-component of the inverter output current i_{oq} to its reference value $i^*_{oq} = 0$.

The block diagram of the inverter q-component control scheme and the open loop transfer functions are shown in Fig. 16. The control scheme includes SRF-PLL loop and current control loop. SRF-PLL loop is controlled by G_{PI-PLL} as introduced in section 2.2 and current control loop is controlled with PI-controller G_{PI} gains which are the same as in previously presented d-component control system. When considering q-component control system the cascaded control scheme is not applied because it is assumed that the DC-voltage control does not affect on the q-component.

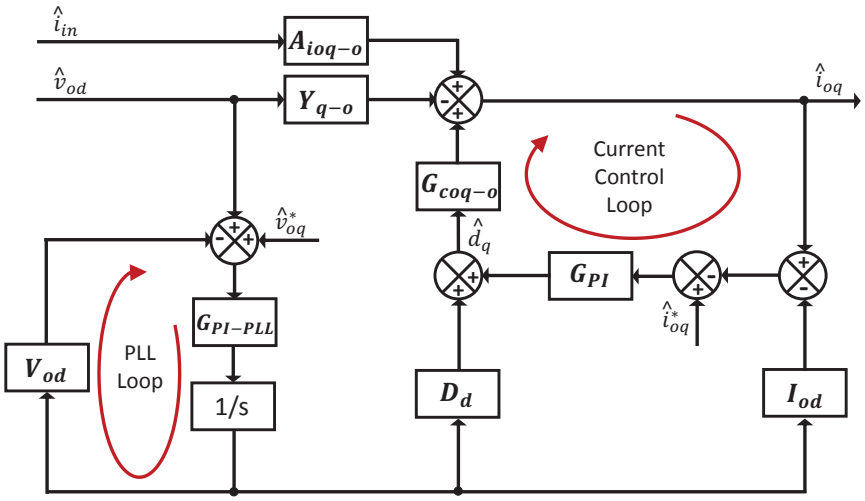

Figure 16: Block diagram of the inverter q-component output dynamics with open loop transfer functions, current control loop and SRF-PLL.

Fig. 16 shows that the phase error $\hat{\theta}$ and thus the output voltage q-component $\hat{v}_{oq}$ have an effect on the sensed output current q-component $\hat{i}'_{oq}$ and the sensed duty ratio $\hat{d}_q$ as also (34) in section 2.2 states. The effects can be written by substituting $\hat{\theta}$ to (38) as

$$\hat{i}'_{oq} = \hat{i}_{oq} - I_{od}\hat{\theta} = \hat{i}_{oq} - \frac{I_{od}}{V_{od}}\left(\frac{L_{PLL}}{(1+L_{PLL})}\right)\hat{v}_{oq} \tag{59}$$

$$\hat{d}_q' = \hat{d}_q - D_d\hat{\theta} = \hat{d}_q - \frac{D_d}{V_{od}}\left(\frac{L_{PLL}}{(1+L_{PLL})}\right)\hat{v}_{oq}, \tag{60}$$

when the ideal grid synchronization is assumed. From (59) and (61) can be seen that phase error $\hat{\theta}$ affects on the current control loop through the steady-state values of the d-component output current I_{od} and duty ratio D_d.

The q-component of the inverter output admittance Y_{out-q} is the transfer function from the output voltage $\hat{v}_{oq}$ to the output current $\hat{i}_{oq}$. The transfer functions can be derived to a simplified form by introducing the SRF-PLL loop gain (36) and current control loop gain defined as

$$L_{out-q} = G_{coq-o}G_{PI}, \tag{61}$$

when PWM and sensor gains are approximated to be unity. The admittance can be derived from Fig. 16 with introduced loop gains as

$$\begin{aligned} Y_{out-q} = -\frac{\hat{i}_{oq}}{\hat{v}_{oq}} =& \frac{Y_{q-o}}{(1+L_{out-q})} - \frac{I_{od}}{V_{od}}\left(\frac{L_{out-q}}{(1+L_{out-q})}\right)\left(\frac{L_{PLL}}{(1+L_{PLL})}\right) \\ & - \frac{D_d}{V_{od}}\left(\frac{G_{coq-o}}{(1+L_{out-q})}\right)\left(\frac{L_{PLL}}{(1+L_{PLL})}\right). \end{aligned} \tag{62}$$

The LCL-filter is also taken account as introduced in (57). The q-component of the output admittance can be then written as

$$Y_{s-q} = Y_{out-q} + Y_C, \tag{63}$$

from which the q-component of the output impedance can be derived as $Z_{s-q} = 1/Y_{s-q}$ which is also considered as source impedance. When considering the shape of the Z_{s-q} it is important to pay attention on the PLL loop gain L_{PLL} because below its crossover the impedance resembles characteristics of the negative resistance $-V_{od}/I_{od}$. The crossover of the current

control loop gain L_{out-q} is usually higher than L_{PLL} and thus the PLL parameters defines the frequency range of the negative resistance like behaviour of Z_{s-q}. Negative resistance in Z_{s-q} hold the phase at -180 degrees (negative sign) and the magnitude constant. This kind of characteristics could produce impedance-based instability at the connection point with the inductive grid if the PLL crossover is too high.

3 Online Grid Impedance Measurements

The grid can be modeled as grid impedance which is also one of the designing parameters for inverter control design. The grid impedance have to be measured for impedance-based stability analysis from actual grid because it is varying over the time.

3.1 Fourier Techniques

According to basic control theory a linear time-invariant system can be characterized by its impulse response $g(t)$. This is illustrated in Fig. 17 where the system is represented as a black box. The impulse response $g(t)$ can be solved by injecting an excitation signal $x(t)$ to the systems and measuring the output signal $y(t)$. By using Fourier techniques time-domain data can be transformed to the frequency-domain. Transformed excitation signal and the system output signal are denoted as $X(\omega)$ and $Y(\omega)$, respectively. Frequency response function can be calculated as

$$G(\omega) = \frac{Y(\omega)}{X(\omega)}. \tag{64}$$

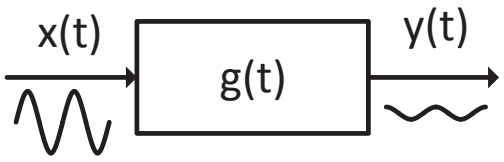

Figure 17: System characterization by its transfer function $g(t)$.

In this thesis the frequency-domain characterization is represented as Bode plots which contains the magnitude and phase shift of the system at different frequencies. Magnitude is represented as decibels which can be calculated as

$$M(\omega) = 20 \times \log_{10}[G(\omega)]\text{dB} \tag{65}$$

and the phase shift as

$$P(\omega) = \arctan[G(\omega)]^{\circ}. \tag{66}$$

3.2 Pseudo-Random Sequences

The PRBS is a broadband binary signal. Hence, it has only two different signal levels in the time domain and it can switch the logical level only after each clock pulse interval Δt [29]. In the frequency-domain PRBS has energy at several frequencies which makes the PRBS-based measurement methods very fast because information of many different frequencies can be collected at the same time.

Maximum Length Binary Sequence

Maximum length binary sequence (MLBS) is the most common form of the PRBS. The MLBS is easy to generate using the system shown in Fig. 18 which includes four shift registers [9] with XOR (exclusive or) feedback from shift registers three and four. The straightforward generation method is one reason why it it so widely used. The MLBS is based on the length $N = n^2 - 1$, where n denotes the number of bits in the applied shift register. In one sequence there are $(N+1)/2$ clock pulse intervals when the signal has one logical level and $(N-1)/2$ intervals when the signal has another logical level [10]. Table 1 illustrates the generation of the MLBS with system and same initial values of the shift registers that presented in Fig. 18.

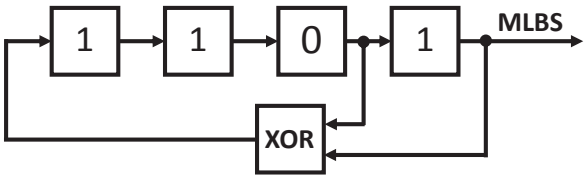

Figure 18: Generation of MLBS with shift registers and XOR feedback.

Logical binary values 0 and 1 are usually mapped to $+a$ and $-a$ where a is the amplitude of the MLBS. This mapping produces symmetrical MLBS with average close zero [30]. Fig. 19 presents two periods of the same MLBS as in the Table 1 generated at 10 Hz. As can be seen from Table 1 MLBS

Table 1: Example of MLBS sequence generated with 4-bit shift register.

Shift	Register 1	Register 2	Register 3	Register 4
1	1	1	0	1
2	1	1	1	0
3	1	1	1	1
4	0	1	1	1
5	0	0	1	1
6	0	0	0	1
7	1	0	0	0
8	0	1	0	0
9	0	0	1	0
10	1	0	0	1
11	1	1	0	0
12	0	1	1	0
13	1	0	1	1
14	0	1	0	1
15	1	0	1	0
16	1	1	0	1
17	1	0	1	0
18	1	1	1	1

is a periodic signal, the same row is repeated after each signal length (here N =15).

Due to the periodicity of the MLBS, the same sequence can be repeated and measurements averaged to reduce the effect of noise [9]. By generating M periods of MLBS the signal-to-noise ratio (SNR) can be increased $\sqrt[2]{M}$ times. Because of these characteristics, the amplitude a of the MLBS can be kept relatively small, and hence, the MLBS is well suited for identifications of sensitive systems which require low-amplitude perturbation. [10]

MLBS have power at certain frequencies $f = q/T$ Hz where T is period of the signal and q is an integer which represents sequence number of the spectral line. The power spectrum of the MLBS signal is given by [7]

$$\Phi_{\mathrm{MLBS}}\left(f = \frac{q}{T}\right) = \frac{a^2(N+1)}{N^2}\frac{\sin^2(\pi q/N)}{(\pi q/N)^2}, \quad q = \pm 1, \pm 2, \ldots \tag{67}$$

where a is the amplitude of MLBS and N is the length of the sequence. As (67) shows the highest value is at the first harmonic ($q = 1$) and then the value drops towards to zero. Fig. 20 shows the power spectrum of the MLBS presented in Fig. 19.

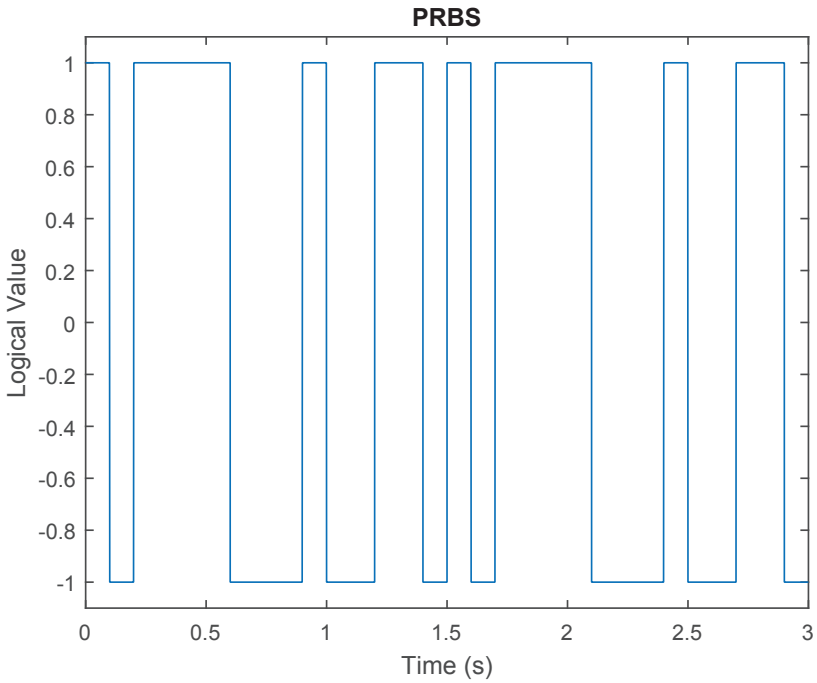

Figure 19: Two periods of 15-bit-length MLBS generated at 10 Hz.

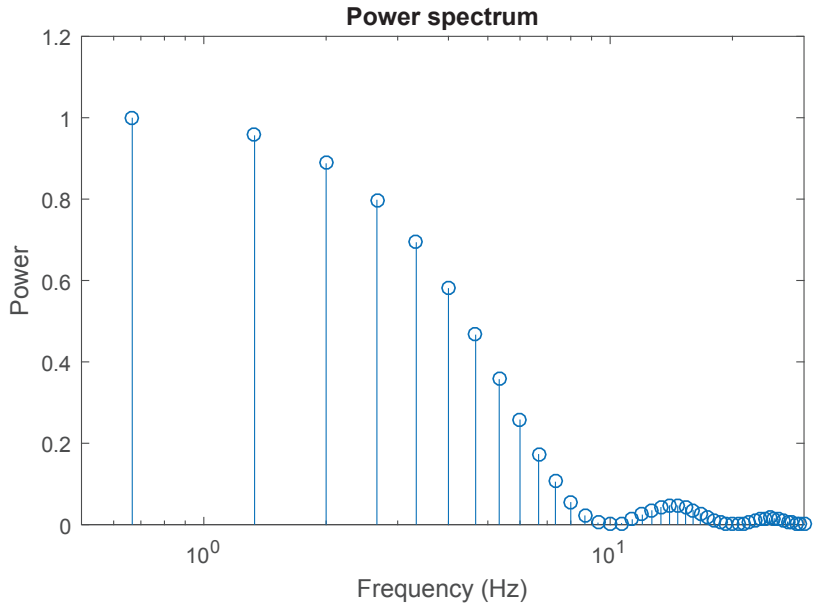

Figure 20: Power spectrum of 15-bit-length MLBS with the $f_{\text{gen}} = 10$ Hz.

To get reliable results of MLBS-based measurements the excitation signal should have approximately equal amount of energy at the all frequencies where the system under test is identified. As can be seen from Fig. 20 the energy content of MLBS drops to half of the energy compared to first harmonic approximately at the frequency of $0.45 \cdot f_{\text{gen}}$. Hence, the bandwidth of the measurements should be limited to that frequency. The bandwidth of the interest is usually known and hence the f_{gen} can be optimized.

The amplitude of the excitation must be kept low enough to avoid nonlinear distortion of the system. The selection of the amplitude requires good understanding of the device under test and varies a lot depending of the device and the measurement conditions. Another way to reduce effect of the noise is to measure multiple periods and then average the results. Measuring M periods the measurement time increases. The measurement time can be solved from $t_{\text{meas}} = NP/f_{\text{gen}}$.

3.3 Grid Impedance and Inductance

Grid-connected systems see the power grid as an impedance Z_g. The shape of Z_g changes with the grid condition. Hence, the modeling of grid conditions can be carried out by estimating the Z_g. The grid inductance L_g is the most critical component to be estimated because it provides information about the weakness of the grid. Grid inductance L_g is shown to be effective variable to describe the grid conditions (i.e. operating conditions for grid-connected systems) for example grid-connected inverters [24], sensitivity analysis of PV systems [31] and feedforward control of grid-connected inverter [32].

It is also important to notice that the increased inductance of the grid leads to increased magnitude at lower frequencies. Due to higher magnitude of the impedance the currents affect to voltages more. That can be a problem because the inverter produces harmonics to the output currents. The harmonic currents affect grid voltage when grid impedance has high magnitude. The grid voltages are fed to the grid synchronization and if the PLL loop has high crossover those harmonics are shown also in the grid phase estimation. The harmonics in the grid phase estimation also leads to affected waveforms of the inverter output currents via current control loop producing more harmonics to the currents. Hence, the harmonics in inverter output current can be repeated in inverter control system if grid inductance is increased.

Measurement of the Grid Impedance

Recently the online grid-impedance measurements have been under extensive research. The measurements have been implemented by various methods for example, by an impulse response method [33], binary sequence test signals [5], sine-sweep analyzer [34], noncharacteristic harmonic currents [35] and oscilloscope data [36]. In this thesis the grid impedance Z_g is measured by using the PRBS-method. The PRBS is injected to the d or q-component current reference signal. Hence, the inverter itself produces the PRBS signal to d or q-component of the grid current (i.e. inverter output current). The impedance is basically a transfer function from current to voltage, and thus, the same component of the grid voltage V_g is measured. By implementing previously presented Fourier techniques the frequency domain impedance is obtained as magnitude $M_g(\omega)$ and phase $P_g(\omega)$ vectors.

Estimation of the Grid Inductance

The power grid is often considered as a resistive-inductive system at low frequencies. Therefore, the grid impedance can be written as

$$Z_g = R_g + j\omega L_g, \tag{68}$$

where R_g denotes the resistive component and L_g inductive component of the grid. This assumption makes the analysis of the grid inductance L_g easier. L_g can be estimated as

$$L_g = \frac{X_g(\omega)}{\omega} = \frac{M_g(\omega) \times sin[P_g(\omega)]}{\omega}, \tag{69}$$

where ω is the angular frequency of the specified frequency point of the impedance Z_g, $M_g(\omega)$ is the magnitude and $P_g(\omega)$ is the phase angle. The grid is assumed to be resistive-inductive only at low frequencies and hence L_g should be calculated from low frequency components of $M_g(\omega)$ and $P_g(\omega)$ to get reliable results.

4 Adaptive Control

4.1 Loop-Shaping Technique

This thesis applies loop-shaping technique for control design. The technique is applied to PI-controllers by setting its zeros, poles and gain to shape the control loop gain. Values of the zeros, poles and gain have different effects on the system transfer functions. Zeros are used to boost phase and thus increasing the phase margin, poles are used to filter out higher frequencies and gain is selected to adjust cross-over frequency. Basically the transfer function with two zeros, two poles and gain can be written as

$$G(s) = \frac{K(\frac{s}{\omega_{z1}} + 1)(\frac{s}{\omega_{z2}} + 1)}{(\frac{s}{\omega_{p1}} + 1)(\frac{s}{\omega_{p2}} + 1)}, \tag{70}$$

where K is the gain ω_{z1} and ω_{z2} are frequencies where two zeros occur and ω_{p1} and ω_{p2} are frequencies of two poles.

Different zeros and poles produce different frequency responses. LHP-zero increases phase by 45 ° in a decade starting from the one decade lower and ending to one decade higher than the frequency where the zero is located thus increasing the phase by 90 ° in two decades. Also the magnitude starts increasing by 20 db in a decade at the frequency where the zero is located. This is illustrated in Fig. 21 with the blue line where the zero is located at 100 Hz. LHP-pole has similar behavior but it decreases phase and magnitude as shown in Fig. 21 with the red line where the pole is located at 100 Hz.

RHP-zero has very similar behavior as LHP-zero but the phase decreases and magnitude increases as shown in Fig. 22. RHP-pole has similar behavior as LHP-pole but the phase increases and magnitude increases as shown in Fig. 22. RHP-zeros cause the dynamics which makes the system to take step-response to a wrong direction first and RHP-pole causes instability.

The gain value K is finally selected after placing the zeros and poles to have desired cross-over frequency. Gain affects only the magnitude of the frequency response and hence the phase has to be adjusted with the use of zeros and poles. The limitation of placing the zeros is that the controller must have at least same amount of poles than it has zeros. Otherwise the controller includes the derivative behavior and is not practicale in real life without filtering. Often in power electronic controllers the zeros are placed

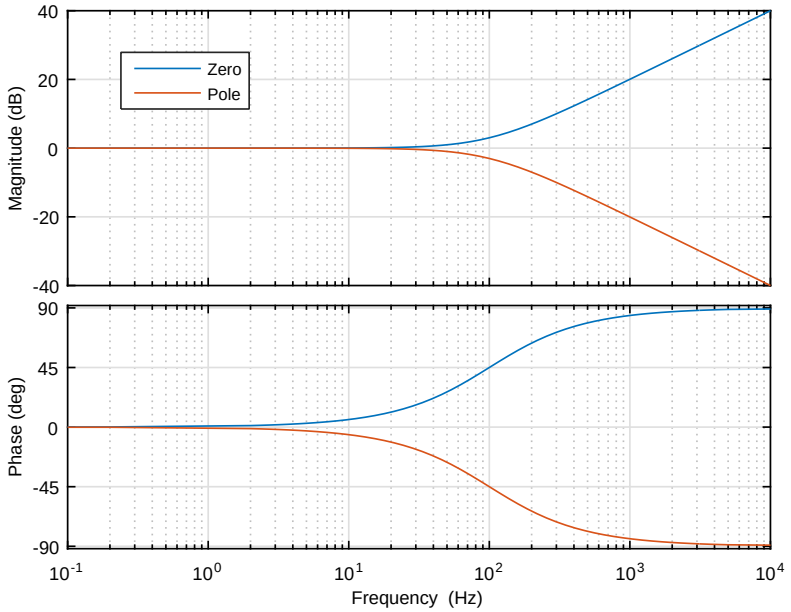

Figure 21: The effect of the LHP-zero and LHP-pole.

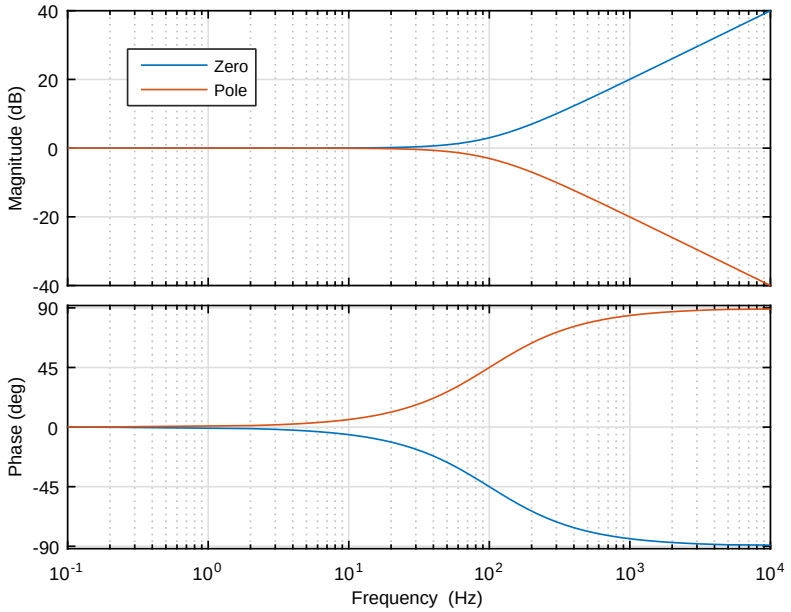

Figure 22: The effect of the RHP-zero and RHP-pole.

at lower frequencies than the poles and thus poles are filtering out the noise and other high-frequency signals.

Effect of Different PLL Parameters

The PLL can be designed with the use of loop-shaping technique. The crossover frequency of PLL should be high enough to have fast dynamics but too high crossover frequency causes instability because of negative resistance like behavior as presented in Section 2.2. The maximum crossover frequency depends on the grid conditions. When grid is more inductive the crossover should be lower because magnitude and phase of the grid impedance increase at lower frequencies. Hence different PLL parameters are designed to have suitable performance to different grid conditions. Also the phase margin should be re-designed when there are different crossover frequencies. Lack of the phase margin produces overshoot or even instability but too large phase margin yields slow performance of the controllers. The PLL is considered as a second order system and the phase margin of 65° represents the optimal value in this case producing relatively small overshoot but fast dynamics.

Fig. 23 represent two different PLL loop gains. They are designed by using loop-shaping technique. It was known that in case of more inductive grid the PLL should have 20 Hz crossover frequency and phase margin of 65° to ensure proper operating in all operating conditions studied in this thesis. When grid is less inductive the crossover frequency can be increased to 167 Hz. The zeros and poles were placed to have suitable phase margin at the crossover frequency which was adjusted with the use of gain. Higher PLL crossover yields better performance but causes instability when grid is inductive.

There is a possibility that grid voltages contain harmonics in their waveforms. The harmonics appears especially in weak grid conditions because of the increased grid inductance as stated in Section 3.2. The harmonics should be avoided in grid synchronization by limiting PLL crossover to the level that attenuates the harmonics. The PLL with 20 Hz crossover is assumed to attenuate all harmonic content from grid voltages. The PLL with 167 Hz do not attenuate the second (120 Hz) and third (180 Hz) harmonics as much as 20 Hz PLL. Hence, there is a possibility that grid phase estimation contains those harmonics.

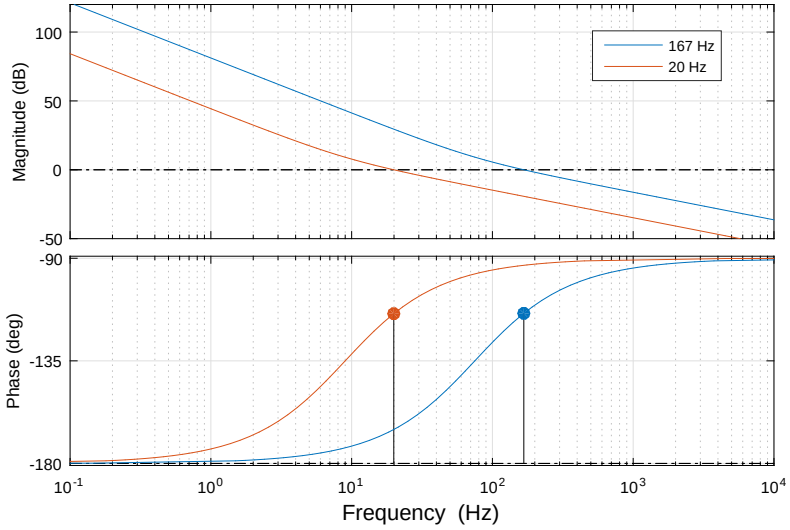

Figure 23: Two different PLL loop gains.

4.2 Gain Scheduling Method

PI-controllers are often designed with constant parameters to be ideal for one specific operating condition. When the operating point or conditions change they affect the control performance. Adaptive controller can modify actual controller behavior by adjusting its parameters to be suitable for the estimated operating condition. Adaptive controller can be seen as two loops as shown in Fig. 24. First loop is basically normal feedback loop with controller, process itself and feedback of the process output. Second loop is controller parameter adjustment loop that changes the actual controller parameters to be suitable for the current operating conditions. [37] In this thesis the gain scheduling method is used to adjust the controller parameters.

Gain scheduling method is based on the estimations of the operating conditions. Often the most difficult part in gain scheduling method design is to define the variables that describe well and simply the operating conditions. When the suitable variables are found the gain scheduling method for adjusting the controller parameters can be implemented by selecting certain parameters for specific operating conditions.

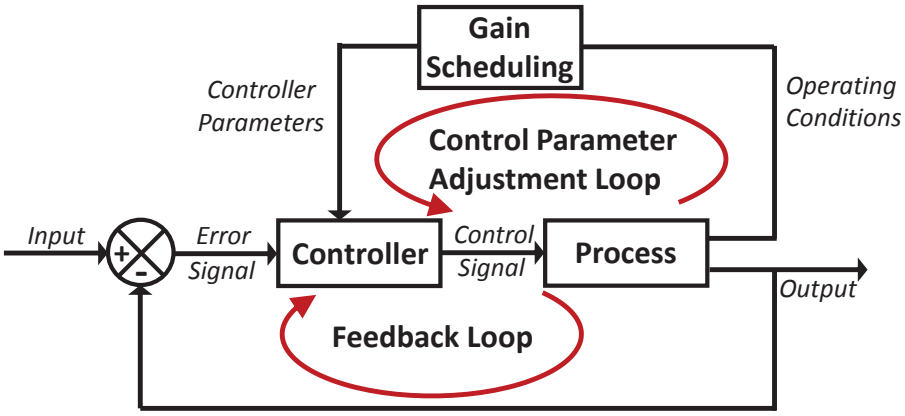

Figure 24: Basic idea of adaptive controllers.

PLL Bandwidth Modification

In this thesis the parameters of the PI-controller parameters of the PLL are adaptively controlled. L_g is used as the variable to describe the operating conditions as presented in Section 3.2. The integral gain K_i and proportional gain K_p are the tuning parameters when optimizing the PI-controller behavior in specific operating conditions.

The crossover frequency ω_{PLL} of the PLL should be optimized such that the PLL is as fast as possible under the current grid condition. If the inductance of the grid L_g increases ω_{PLL} should be reduced to ensure stability. That is because the increased magnitude curve of the inductive grid overlaps the inverter magnitude curve at the lower frequency. The PLL affects the impedance of the inverter q-component, and thus, the phase angle stays at -180 degrees below PLL crossover frequency (negative resistance). Hence, if ω_{PLL} is higher than the frequency where the grid and inverter have the same magnitude, then there is possibilities that the phase difference between the grid and the inverter is over 180 degrees. That is considered as impedance-based instability as presented in Section 2.5. When the inverter is modeled analytically for different behaviors of the adaptively controlled PLL, the adaptive control should make sure that ω_{PLL} is suitable for current grid condition and attenuate the possibly harmonic

In this thesis two different PLL loop gains are tuned. The loop gains are presented in Fig. 23. The PLL with 20 Hz crossover is tuned to have proper operating in inductive grid conditions and PLL with 167 Hz crossover produces faster dynamics and is implemented when there is less inductive grid. Fig. 25 shows inductive grid impedance and inverter output impedances with 20 Hz

and 167 Hz PLL. It can be seen that there is a possibility of impedance mismatches yeilding instability when PLL has higher crossover. The instability is avoided when the PLL crossover is decreased to 20 Hz. The lower crossover affects the phase curve of the inverter output impedance by increasing it at lower frequencies and thus the phase difference with the inductive grid is less than 180 degrees at the frequency where magnitudes overlap. Switching between applied PLLs is implemented using gain scheduling method by multiplying the gains of the PI-controller with specified constant. For the 20 Hz PLL the gains are: $K_{p-20} = 0.672$ and $K_{i-20} = 38.019$. For 167 Hz PLL the gains are: $K_{p-167} = 5.711$ and $K_{i-167} = 2512.900$. The constant for adaptive gain scheduling is for proportional term $\frac{K_{p-167}}{K_{p-20}} = 8.499$ and for integral term $\frac{K_{i-167}}{K_{i-20}} = 66.096$. First the 20 Hz PLL is implemented in the control system and it can be switched to 167 Hz PLL by adaptively multiplying PI-controller gains by specified constants. Value of L_g defines the PI-controller gains. The control parameter adjustment loop of the adaptive controller (shown in Fig. 24) activates the multiplier of the PI-controller gains when L_g is decreased below specified limit and deactivates it when L_g is increased above that limit. The limit of L_g is set to 2 mH in experiments because 167 Hz PLL provides proper operating below that value.

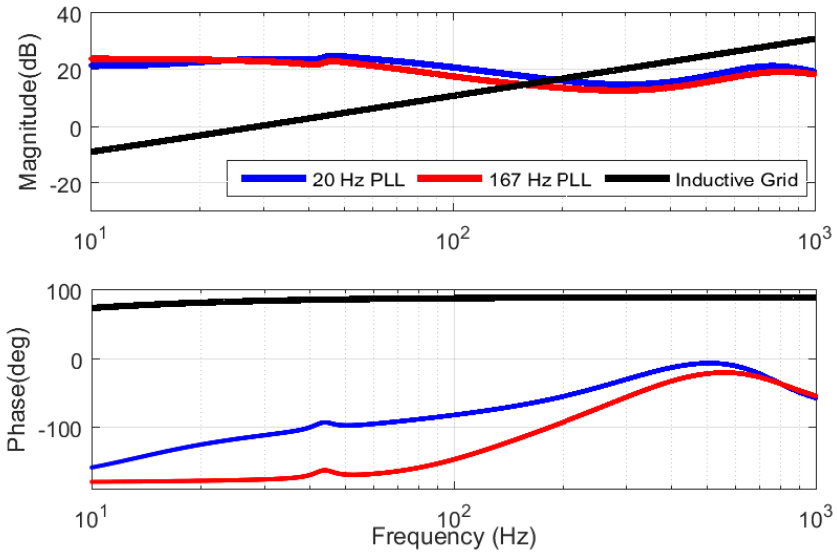

Figure 25: Inverter output impedances with two PLL loop gains and inductive grid impedance.

5 Experimental Results

5.1 Power Hardware-in-the-Loop Tests

It is very hard and complex to model real-world conditions in a basic software-based simulation. Simulations are still very useful tool for designers to test new control ideas. Hence, it is attractive to build testing systems that can replicate real-world conditions but also provide easy way to test new ideas. Power hardware-in-the-loop (PHIL) tests combine the real devices and simulators by replacing the device under test by an actual hardware [38]. In this thesis the grid and the control system of a real inverter is simulated with use of dSPACE which is a real-time simulator.

dSPACE runs c-code continuously and provides real-time interface for the inverter control system and grid emulator with the use of its I/O board. This makes it possible to change inverter controller parameters and grid characteristics online without disconnecting the system. This helps when time-varying grid conditions are modeled and stability of the system is considered. Matlab/Simulink provides a tool that generates a c-code automatically from Simulink model. Hence, the whole system can be modeled with the use of Simulink models and the dSPACE runs the modeled control system of inverter. dSPACE has proven to be effective tool for the design in many applications including digital controls for power electronics [11], three-phase photovoltaic inverter [39] and back-to-back converter [40].

In this thesis a method where the real-time impedance measurements runs parallel with inverter control system is implemented to the dSPACE. The method does not require any other signal generators or measurement devices. Only dSPACE is needed to run control system and measure desired frequency responses. Real grid-connected inverter itself can produce the measurement signal by changing the duty ratios d. Inverter can also use its own voltage and current sensors to measure the grid impedance.

dSPACE Implementation for Real-Time Grid Impedance Measurements

Fig. 26 shows the MLBS injection generation block diagram. The MLBS is generated with n shift registers and XOR feedback. The generation produces MLBS with two logical levels 0 and 1. The amplitude K of the injection can be changed. The amplitude is amplified by two (gain block) and then summed

$-K$ to produce injection with logical levels of $-K$ and K. Hence, amplitude of the injection is K and the time-domain average (bias) is close to zero.

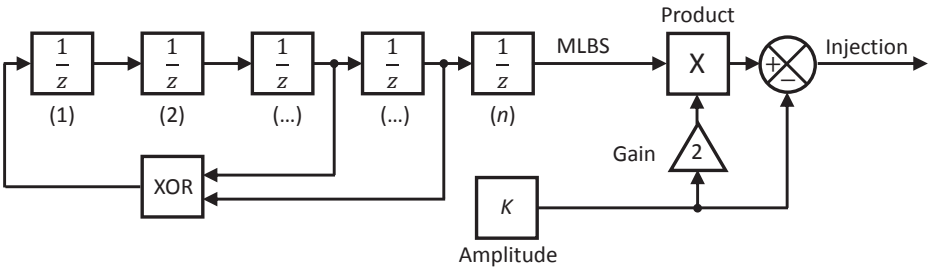

Figure 26: Diagram of the MLBS generation.

The excitation from the MLBS generator (shown in Fig. 26) is injected to the system under test using output terminal of dSPACE I/O board. The injection $x(t)$ and the system response $y(t)$ are measured with input terminals of I/O board. The effect of noise is reduced by averaging data over P periods. The averaging procedure is illustrated in the Fig. 27. Delay blocks delay their time-domain input signals by one period to get data from past periods for averaging procedure.

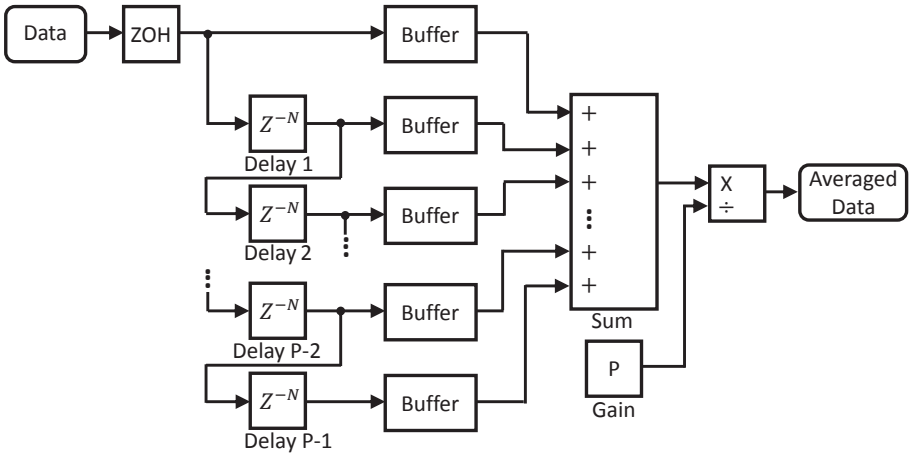

Figure 27: Diagram of the averaging procedure.

The averaged time-domain data is transformed to the frequency-domain by using discrete Fourier transform (DFT). The frequency-domain injection is denoted as $X(\omega)$ and the system response is denoted as $Y(\omega)$. The frequency response function $G(\omega)$ is calculated as in (64). Magnitude and phase angle of the system are calculated from complex $G(\omega)$ to produce Bode plot.

Bode plot can be seen in the dSPACE control desk continuously. The simplified implementation to measure grid impedance Z_g in frequency domain as magnitude $M_g(\omega)$ and phase $P_g(\omega)$ vectors is shown in Fig. 28.

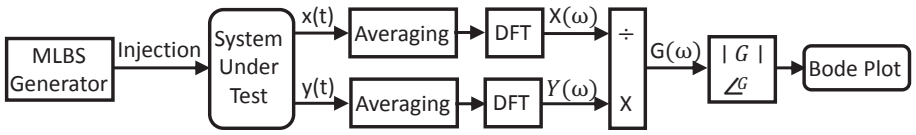

Figure 28: Grid impedance measurement block diagram using MLBS injection.

When the measurements are carried out with the use of the MLBS method, the imaginary components of the impedance measurement vector can be divided by the specified frequencies of the MLBS to get inductance value. Numerical value of the grid inductance can be calculated from imaginary component of the grid impedance as (70). Fig. 29 shows the procedure that calculates the numerical value of the grid inductance from frequency response measurements of the grid impedance.

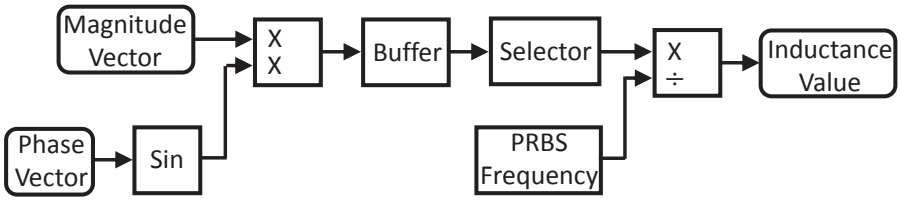

Figure 29: Diagram of the procedure that calculates inductance from frequency response results.

5.2 Experimental Setup

The picture of the experimental setup in the laboratory is shown in Fig. 30 and the block diagram of it is shown in Fig. 31. The setup includes grid emulator, PV-simulator, inverter with output filter and dSPACE model 1103 with I/O board as a control system. An isolation transformer is connected between the inverter and grid emulator to provide galvanic isolation between the inverter and grid emulator to attenuate common mode currents which could break the PV-simulator. The grid emulator acts as an AC-load of the system. The PV-simulator is the DC power source for the system. The inverter transforms the DC-valued power to the suitable AC-valued power to the grid. The inverter has no integrated control system and hence the control system is implemented with the use of dSPACE which controls also the grid

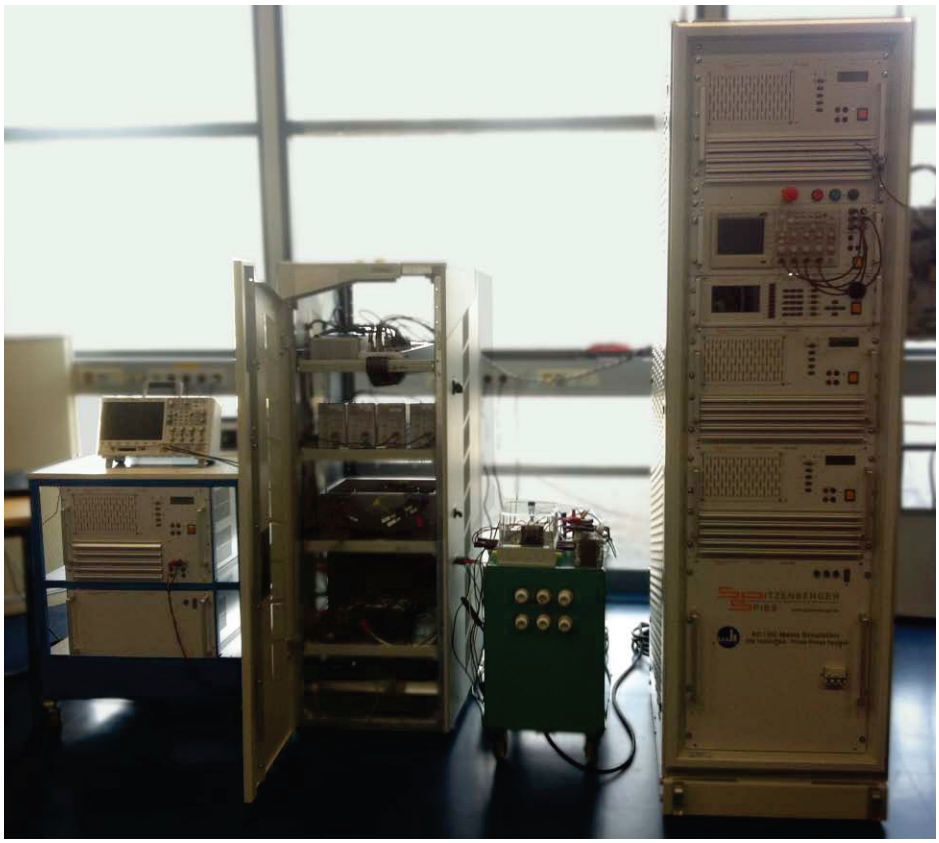

Figure 30: Experimental setup.

emulator and PV-simulator. The measurements are also implemented with the use of the inverter and dSPACE as shown previously in Section 4.1.

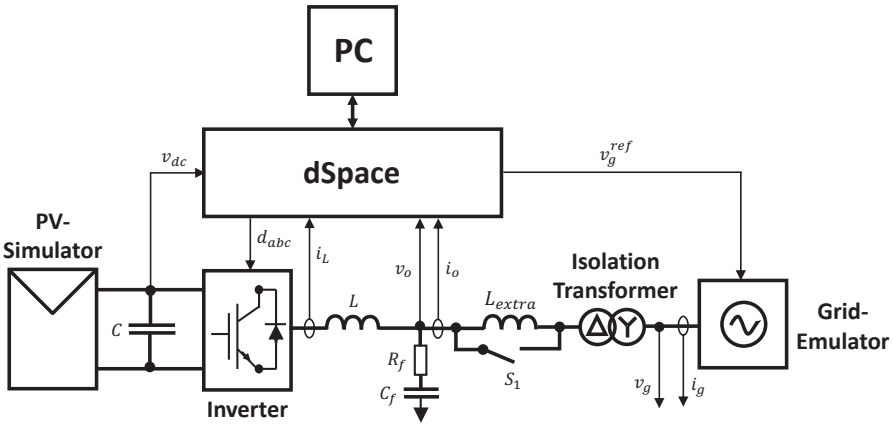

Figure 31: Block diagram of the experimental setup.

The grid emulator is Spitzenberger Spies PAS 15000 Grid emulator. It consists of three 4-quadrant linear amplifiers, integrated control system and an oscilloscope showing the waveforms. In these experiments the device repeats the reference voltages generated by dSPACE. The grid emulator could act as source or load for the system but in this thesis the emulator is used as a load only. Acting as a load the system does not require any additional resistive loads, just grid emulator. To model different grid conditions the extra inductor L_{extra} of 3 mH or 5 mH is connected to series between the inverter and isolation transformer. The inductors can be bypassed to model fast changing conditions with the use of relay that is modeled in Fig. 31 as switch S_1. Also the isolation transformer is assumed to add 0.6 mH inductance to grid impedance.

PV-simulator is a 3 kW photovoltaic generator manufactured by Spitzenberger Spies. It has controllable IV-curve which illustrates the real-world functioning of the PV-generator in different conditions. In these experiments only one very simple IV-curve is used and the maximum power point (MPP) is achieved by adjusting the reference signal v_{in}^* for the DC-voltage control to the MPP-voltage by hand in dSPACE.

The studied inverter is model Myway Plus MWINV-9R144 manufactured for the power electronic research. It is basically IGBT inverter which own control system can be replaced by real-time simulator (like dSPACE). The inverter includes capacitors at the DC-side and can be thus modeled as presented in Section 2.1. The control system of the inverter is implemented with the use of Simulink model by using controllers presented in Section 2.2. There is also

LC-type low-pass filter connected to the output of the inverter. It is used to attenuate switching ripple of the output current of the inverter. The effect of the filter is denoted as C_f and R_f in Fig. 31.

5.3 Impedance-Based Stability Analysis

The inverter has to be modeled in certain steady-state operating point when considering the small-signal model derived in Section 2.1. Parameters of the inverter steady-state operating point is shown in table 2 when the PV-generator is operating at MPP. The ideal grid synchronization is desired and thus the q-component of the grid current is regulated to zero.

Table 2: Parameters of the inverter.

V_{in}	414.3 V	V_{od}	$\sqrt{2}$ 120 V	L	2.2 mH	ω	2 π 60 rad/s	I_{oq}	0 A
I_{in}	6.577 A	V_{oq}	0 V	C	1.5 mF	r_e	0.1 Ω	f_{sw}	12 kHz

Output Impedance of the Inverter

The output impedances are calculated from analytical model as presented in Section 2.3. The control system is implemented as presented in Section 2.2 and included to the small-signal model presented in Section 2.1 with parameters of table 2.

The DC-voltage control loop L_{in} is tuned to have crossover at 6 Hz and phase margin of 60 degrees. The current control loops of d and q-components applies same PI-controllers and L_{out-d} is tuned to have 509 Hz crossover and L_{out-q} 506 Hz crossover both having phase margin of 65 degrees. The different PLL loop gains applied are introduced in Section 3.3 and they are adaptively controlled to be suitable for current operating conditions. Fig. 32 shows the d-component of the inverter output impedance calculated with introduced method. The PLL is adaptively controlled in this thesis and as presented previously the parameters of PLL does not affect on the d-component of the inverter output impedance. Thus the d-component is not under actual research in this thesis.

Two different PLL loop gains are derived in Section 3.3 and are shown in Fig. 23. The effect of the PLL loop gain crossover frequency to the output impedance can be seen when comparing Figs. 33 (20 Hz crossover) and 34 (167 Hz crossover), the phase stays close to -180 degrees and magnitude

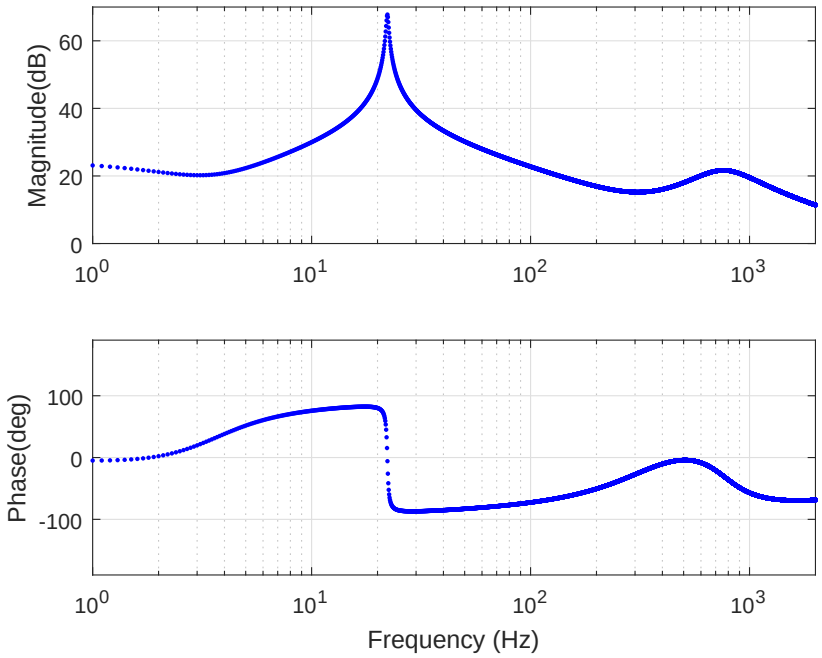

Figure 32: D-component of the inverter output impedance.

constant to the higher frequencies when crossover of the PLL loop gain is increased. That negative resistance like behavior at higher frequencies implies the system to be more sensitive for inductive loads. Weak grid conditions are usually represented as increased inductance in grid impedance. It may be obvious that inverter output impedance with lower crossover of the PLL loop gain is more suitable for weak grid conditions. The increased crossover still yields faster dynamic responses and thus is preferred in normal conditions.

Continuous Grid Impedance Measurements

The grid impedance is measured from the actual grid using nonparametric methods. In this thesis the impedance is measured from the grid emulator using MLBS-based method implemented in the dSPACE as presented in Section 4.1. The generated MLBS is included to the reference signal of the inverter current control loop. The amplitude of the MLBS has to be limited because it affect the current waveform. By experimental test the amplitude K of the MLBS was set to 0.5 A which does not affect significantly to the current quality and still provided reliable results. The grid current and voltage are measured and by computing their ratio the frequency domain grid impedance is obatined. This procedure is repeated continuously as presented.

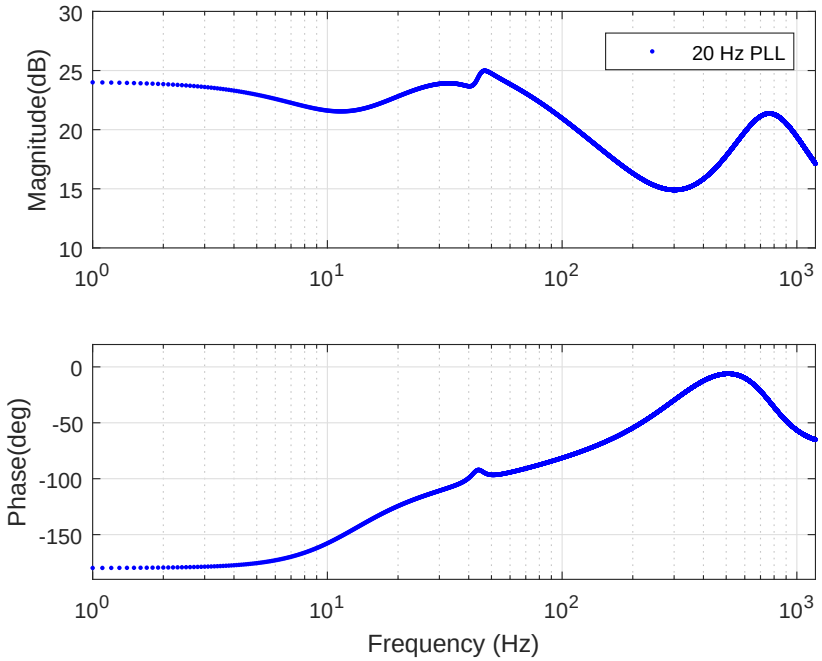

Figure 33: Q-component of the inverter output impedance when PLL has 20 Hz crossover.

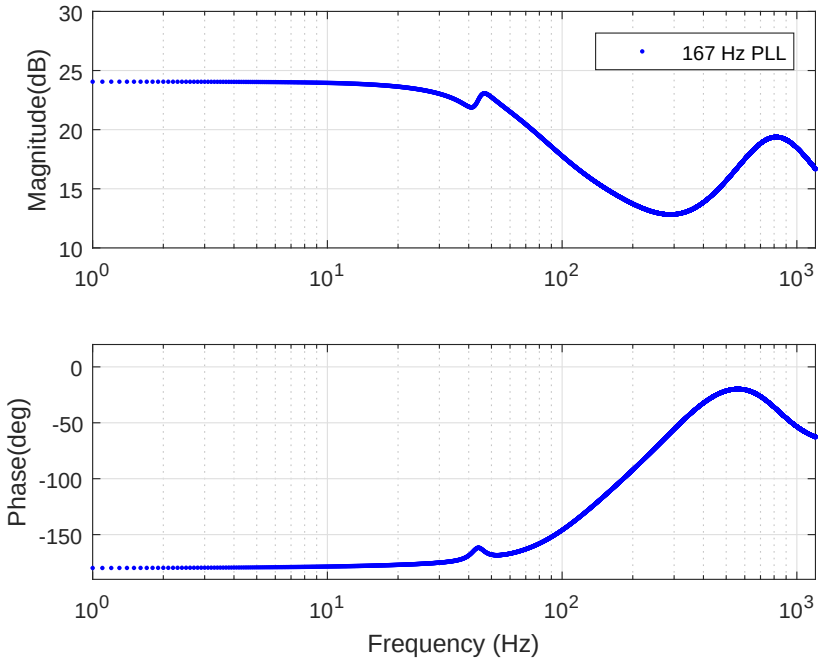

Figure 34: Q-component of the inverter output impedance when PLL has 167 Hz crossover.

When using 127-bit-long MLBS and 4 kHz generation frequency, the measurement cycle is approximately 0.38 s yielding 31 Hz refresh rate for the new impedance result.

Fig. 35 shows the grid impedance in three cases. The grid impedances can be seen in the dSPACE control desk continuously. The blue line represents the strong grid operation which is affected by only the internal impedances of the grid emulator and isolation transformer. The isolation transformer adds approximately 0.6 mH inductance. The red line represents a more inductive grid which includes a series-connected 3 mH inductor. That represents slightly weak grid conditions. The black line represents very weak grid conditions and there is 5 mH extra inductor connected per phase in series with isolation transformer.

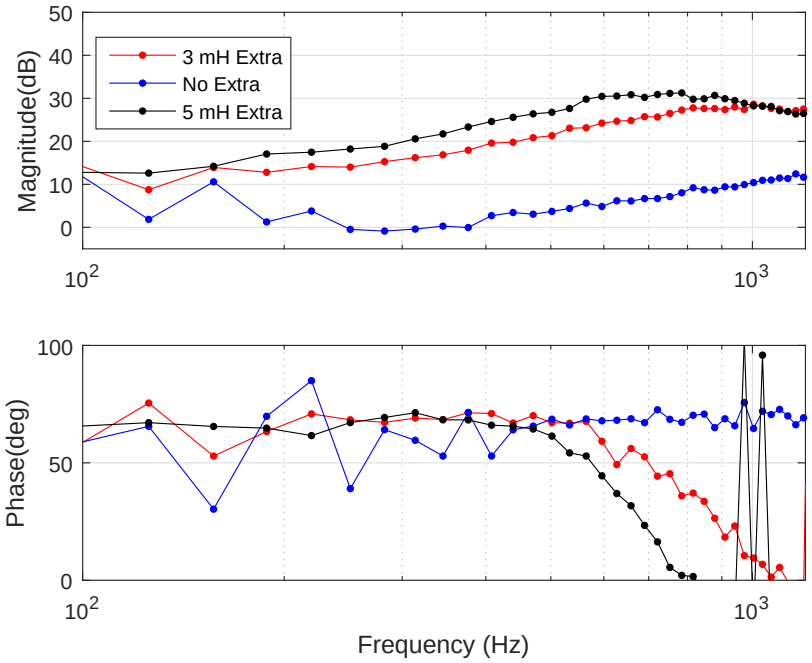

Figure 35: Grid impedance measurement.

When considering grid impedance at low frequencies it is assumed that inductive element is dominating. Pure inductance and small series resistance should produce the phase shift close to 90 degrees. Fig. 35 shows that measured phase shift of the grid impedances is not increased to 90 degrees and stays close to 60 degrees. When assuming the grid impedance to be inductive in low frequencies, the measurements underestimates the phase shift.

Continuous Grid Inductance Measurements

The suitable parameter for adaptive control is grid inductance L_g which describes the grid conditions in a simple and reliable way. The approximation of the grid inductance can be calculated from the measured grid impedance in dSPACE as presented in Fig. 29. The theory and equations are provided in Section 3.2. The new inductance value is approximated from every impedance measurement and thus the measurement cycle is 0.38 s.

Fig. 36 is the real-time inductance measurement result when the grid is considered to be strong. The inductance results are taken at the same time as the impedance value in Fig. 35 (blue line). Hence, the internal inductance of the grid emulator and isolation transformer are measured. The inductance of the grid emulator is small enough to be neglected but isolation transformer includes about 0.6 mH inductance. Based on these assumptions the measurement system underestimates the value of inductance but still provides good enough results to implement adaptive control. That underestimation is due to impedance measurement in which the phase shift did not increase over 60 degrees when it was assumed to increase close to 90 degrees. Fig. 36 shows the result of continuous inductance value monitoring where blue line represents non-averaged result and red line averaged results which is averaged over past six measurements to attenuate the ripple. The averaged results have less than 0.05 mH peak-to-peak ripple when the non-averaged have almost 0.2 mH peak-to-peak ripple.

Fig. 37 is the inductance measurement from the same time when the impedance in Fig. 35 (red line) is measured. Now the 3 mH extra inductor is added series with the isolation transformer to each phase. Hence, the total inductance should be around the 3.6 mH. The measurement system underestimates the inductance again but the difference in average inductance compared to the value in Fig. 36 is very markable and thus the measurements can be fed to the adaptive controller.

Fig. 38 represent the fast increasing inductance in the grid i.e. the grid becomes weak suddenly. The inductance starts increasing at 0.25 s. The non-averaged measurement rise time is much faster (approx. 0.2 s) than the averaged result (0.4 s). Measurement setup can be seen from Fig. 31 where the extra inductor L_{extra} is just a normal inductor which can be bypassed with switch S_1. Increased inductance is implemented by turning the switch off a the time of 0.22 s.

Fig. 39 represents situation in which the grid suddenly becomes strong again.

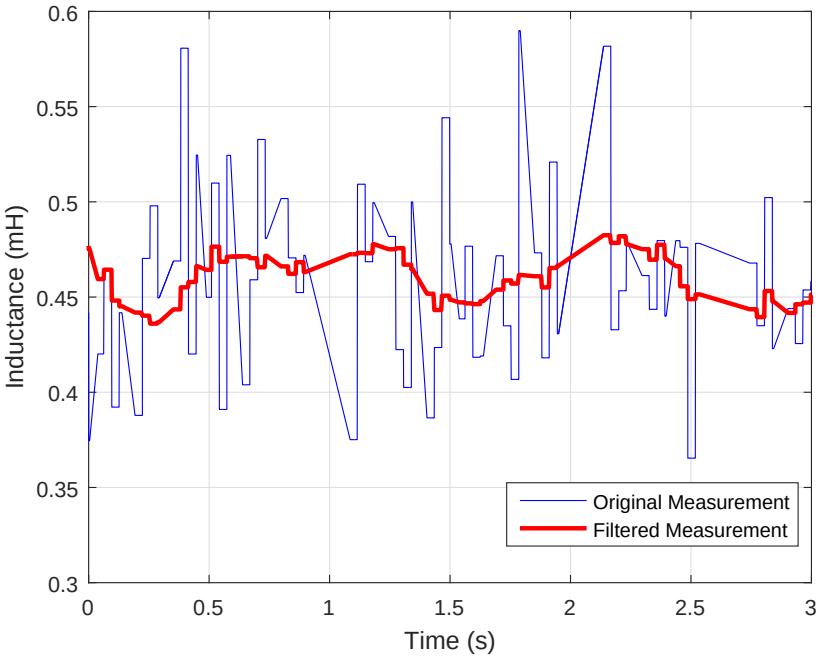

Figure 36: Grid inductance measurement with low inductance values.

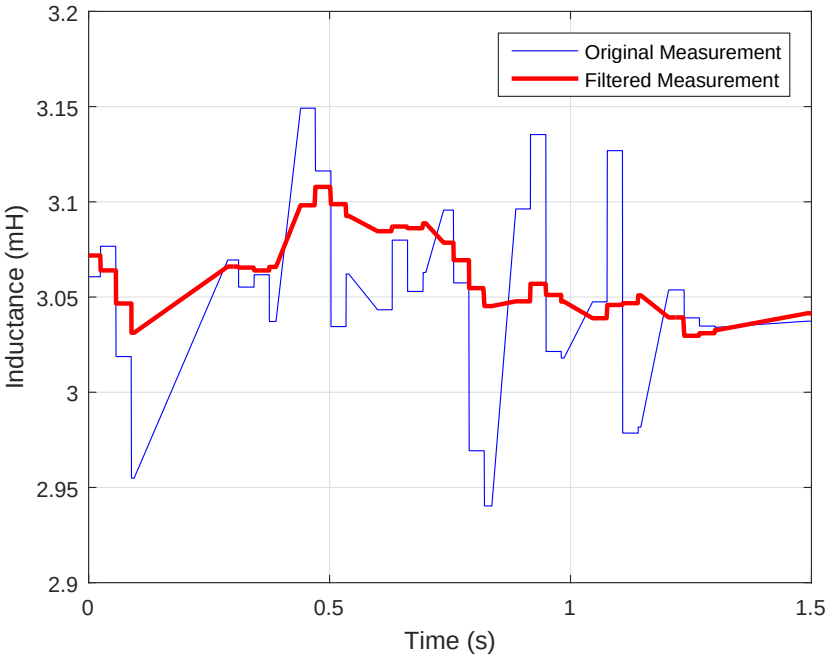

Figure 37: Grid inductance measurement with high inductance values.

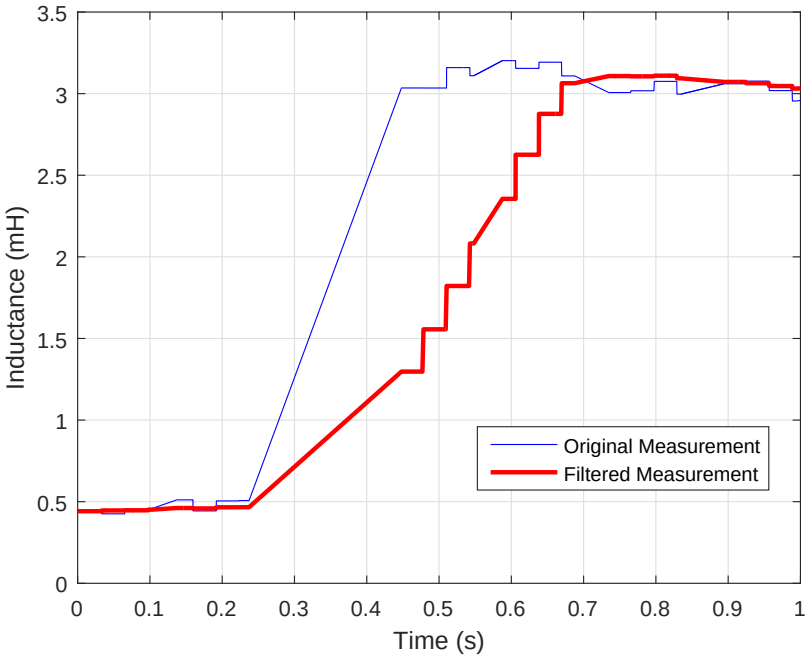

Figure 38: Grid inductance measurement when the inductance value is increasing suddenly.

This is implemented similar way as the increasing inductance. The switch S_1 is turned on at the time 0.25 s. Results are also similar with the increasing inductance, the fall time for non-averaged is approx. 0.1 s and for averaged 0.3 s.

When considering the measurement results from Figures 36 - 39 it can be seen that the averaging attenuates ripple but slows down the rise and fall time when inductance is changing. More accurate results are chosen to represent the grid conditions and thus the averaged results are used to implement adaptive control. In experimental tests the non-averaged inductance had great peaking sometimes which is not acceptable when the measurement results are fed to the adaptive controller. Peaking in the inductance measurements would affect to the adaptive controller by switching the adjusted parameters without actual purpose. The averaging attenuates the peaks and thus decrease unnecessary switching between different parameters.

Impedance-Based Stability Analysis

As presented in the Section 2.5 the impedance-based interactions occur at the certain resonance frequency f_r. The frequency is located when the inverter

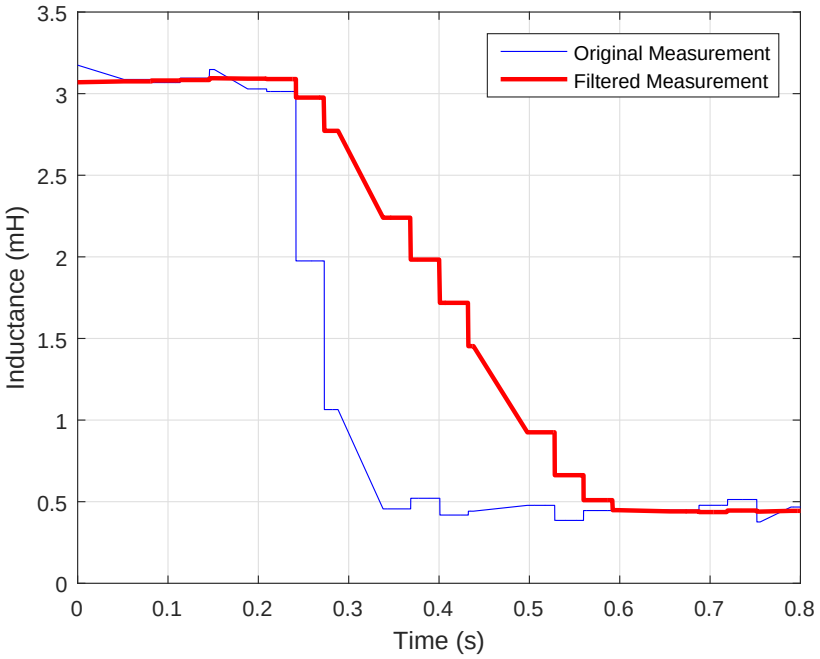

Figure 39: Grid inductance measurement when the inductance value is decreasing suddenly.

output impedance Z_s and grid impedance Z_L have the same magnitude and the phase difference is more than 180 degrees. The phase A output current from the inverter is measured with the use of an oscilloscope. The fast Fourier transformation (FFT) is applied and frequency content of the currents is measured. Fig. 40 represent unstable current in the frequency domain. There are significant amplitudes in the dq-domain at two frequencies. Those frequencies are $f_r + 60Hz$ and $f_r - 60Hz$. That 60 Hz frequency variation appears because of Park's transformation. The real resonance frequency can be calculated to occur at 149 Hz in time-domain. That frequency is not close to a any harmonics that could appear in 60 Hz grid. Thus the source of instability is considered as impedance mismatches in the connection point of the inverter and grid.

The impedance of the grid is measured at the same time when unstable current occurs. Fig. 41 shows the measured grid impedance (blue line) and analytical q-component of the inverter output impedance (red line). Figure is zoomed close to the predicted resonating frequency shown in Fig. 40 to ensure that the impedance mismatches are the source of instability. The analytical inverter output impedance contains the PLL with 167 Hz crossover and the impedance is shown in Fig. 34. Also the analytical grid impedance

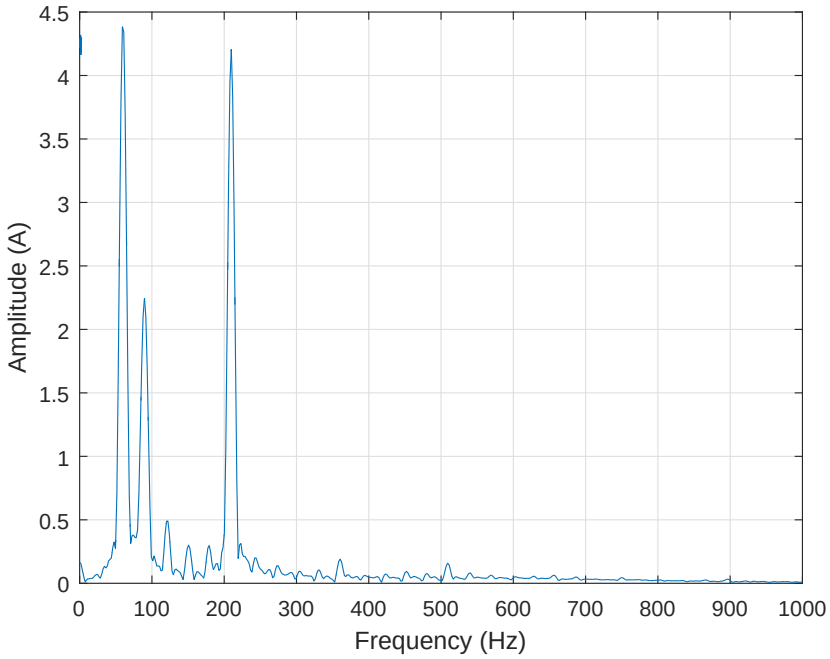

Figure 40: Unstable current in frequency domain.

(black line) is shown. The analytical grid impedance was calculated when it was assumed that total inductance is approximetely 5.6 mH (5 mH extra inductor and 0.6 mH isolation transformer) and resistance of the grid was approximated to be 0.1 Ω. The magnitudes of analytical and measured grid impedances have similar shape and both overlap the analytical inverter output impedance at the frequency of 158 Hz. The phase at 158 Hz of the measured grid impedance is 66 degrees and the analytical grid impedance estimates the phase of 89 degrees. The phase at 158 Hz of the inverter output impedance q-component is -112 degrees. Thus the phase difference between measured grid impedance and inverter output impedances is 178 degrees which indicates still stable dynamics. When the grid impedance curves in Fig. 35 was analyzed it was considered that implemented measurements based on MLBS underestimates the phase shift. The phase shift between analytical grid impedance and inverter output impedance is 201 degrees which indicates unstable dynamics as assumed based on the current FFT results.

Based on the impedance curves the system should resonate at the frequency of 158 Hz where impedances overlap. The resonance in grid currents nevertheless occurs at the frequency of 149 Hz based on the FFt data from Fig. 40. The error in frequency is still quite small and can be the result of differences between the actual inverter dynamics and the analytical model. Real-world

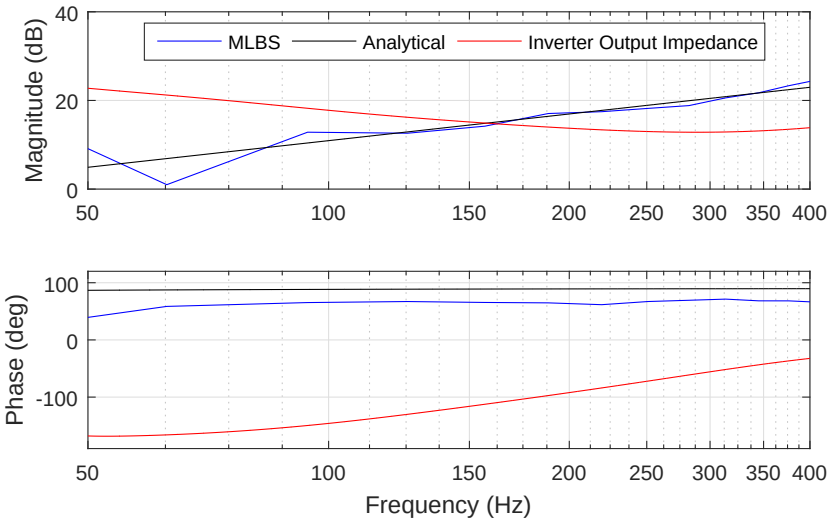

Figure 41: Grid impedance and inverter output impedance in unstable case.

operations includes many uncertainties and analytical model some assumptions and thus the small errors occur.

Fig. 42 shows the phase A grid current FFT when 3 mH extra inductor is connected to the grid side and PLL with 167 Hz crossover is applied in inverter control system. The conditions are thus the same as in previous case but the grid side extra inductance is decreased from 5 mH to 3 mH yielding less weak grid conditions. There are significant amplitudes in grid current FFT at the frequencies of 120 Hz and 240 Hz. That implies the problems at the frequency of 180 Hz which is third harmonic in 60 Hz grid. In this case the connection point is not necessarily unstable but amplifies the third harmonic.

Fig. 43 shows the measured grid impedance (blue line) and analytical q-component of the inverter output impedance (red line). Also the analytical grid impedance is shown (black line) when it was assumed that total inductance is 3.6 mH (3 mH extra inductor and 0.6 mH isolation transformer) and resistance of the grid was approximated to be 0.1 Ω. The analytical inverter output impedance contains the PLL with 167 Hz crossover which impedance curve is shown in Fig. 34. The magnitude behavior of measured and analytical impedance have very similar shape both overlapping the inverter output impedance at frequency of 210 Hz. The phase at 210 Hz of the measured grid impedance is 70 degrees and the analytical grid impedance estimates the phase of 89 degrees. The phase at 210 Hz of the inverter output impedance q-component is -84 degrees. That yields the phase difference of 154 degrees

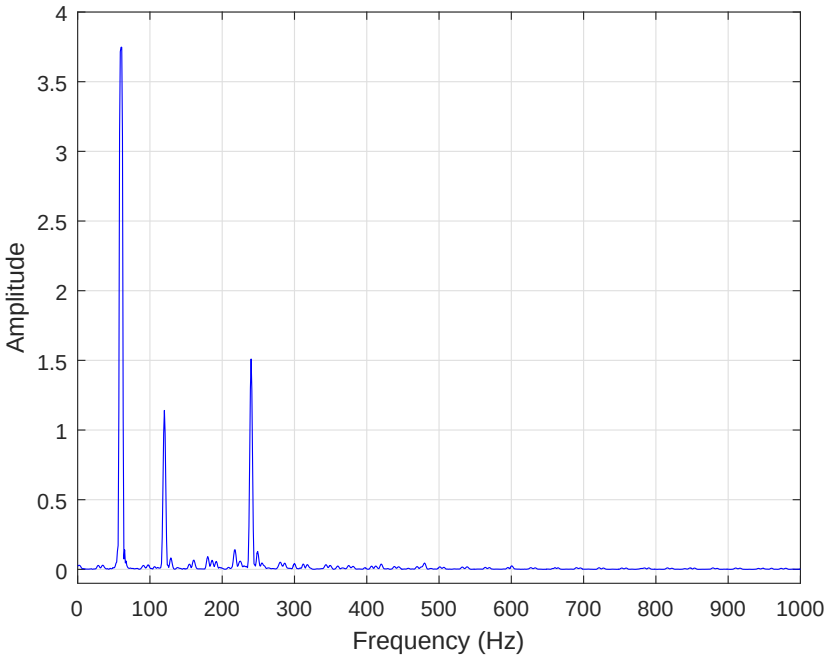

Figure 42: Current with harmonic content in frequency domain.

between measured grid impedance and inverter output impedance and 173 degrees between analytical impedances. This represents stable operation and there are no impedance mismatches and thus the poor waveforms are not a result of unstable connection point of inverter and grid.

It can be seen from Fig. 35 that increased inductance of the grid yields increased magnitude of grid impedance at lower frequencies. As presented in Section 3.2 due to higher magnitude in grid impedance the harmonic content can be also seen in grid voltages. When PLL has crossover of 167 Hz the third harmonic (180 Hz) in grid voltages affects the phase estimation (as predicted in Section 3.3) which leads to repeated effect of the harmonic content. This kind of repeated effect of the harmonics leads to grid currents as Fig. 42 represents.

5.4 Adaptive Control

The adaptive control is implemented by PLL bandwidth modification as presented in Section 3.4. The adaptive control system is included to the inverter control system, the grid inductance measurements are performed with the use of MLBS methods and whole system is tested in different operating condi-

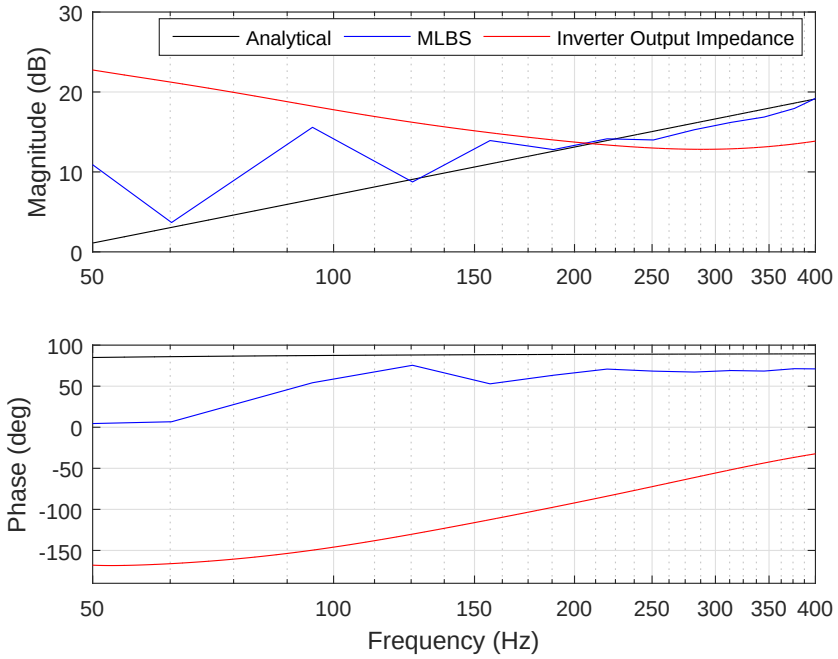

Figure 43: Grid and inverter output impedances with low phase margin.

tions by PHIL-test as presented in Section 4.1.

Power Quality Improvement

The adaptive control system was tested when 3 mH extra inductor was suddenly connected in series to the grid side. That represents the increased inductance in grid. The output current FFT in the same situation with 167 Hz PLL is shown Fig. 42. The same kind of harmonic content is predicted to occur when extra inductance is connected.

Fig. 44 shows the phase A output current, inductance measurement and also the control signal (black line) of the adaptive control system at the time of increased grid inductance. When control signal has the rising edge the adaptively controlled PLL bandwidth modification is switched the 167 Hz PLL to 20 Hz. At 0.1 s the extra inductance is connected. As can be seen the output current is directly weakened and also the measured inductance value started directly to increase. After approximetely 0.3 s the adaptive controller reacts to the increased grid inductance by switching PLL parameters. Directly after switching PLL parameters the waveform of the output current is recovered and the control system is adapted to the increased grid inductance.

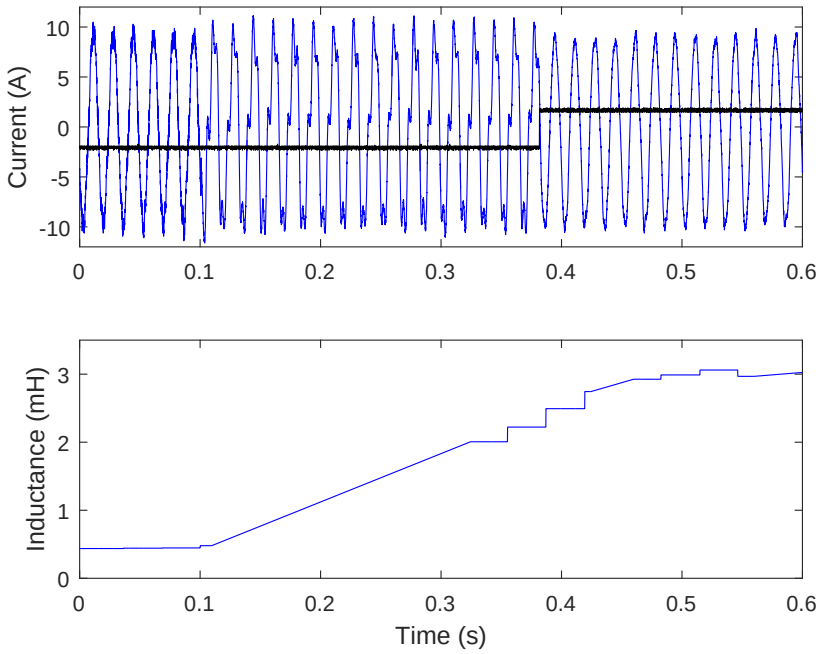

Figure 44: Adaptive control results when grid inductance is increased.

Fig. 45 shows the test results closer to the point in which the extra inductance is connected. Before 0.1 s the current has rather pure sinusoidal waveform containing only some high frequency error which is a result of MLBS-based measurements in which the MLBS is included to the inverter output currents. At 0.1 s the extra inductance is connected and the effect of it can be clearly seen from the current waveform. The current contains significant amount of third harmonic after 0.1 s as predicted and shown in Fig. 42.

Fig. 46 shows the test results closer to the point in which the adaptive control reacts to increased grid inductance and the waveforms of inverter output current is recovered. The inductance value reaches the limit of 2 mH at 0.32 s in which the adaptive control should react and decrease the PLL crossover to 20 Hz. The control signal has rising edge at 0.38 s and thus the internal delay of the PLL bandwidth modification is approx. 0.06 s. Hence, the PLL parameters are switched to the suitable for inductive grid at 0.38 s. After the switching of parameters the waveform of current is directly recovered and have quite pure sinusoidal shape containing the MLBS. The MLBS have decreased effect on the waveform compared to the situation in which the extra inductance was not connected (before 0.1 s). The decreased effect is due to basic influence of the inductance to the current which acts as a low-pass filter for switching harmonics.

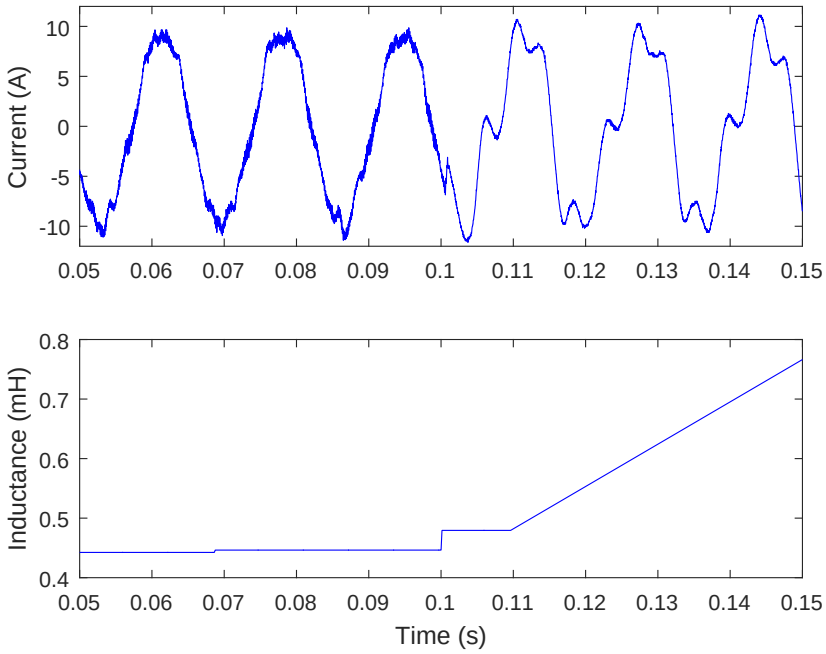

Figure 45: Currents and inductance when extra inductance is connected.

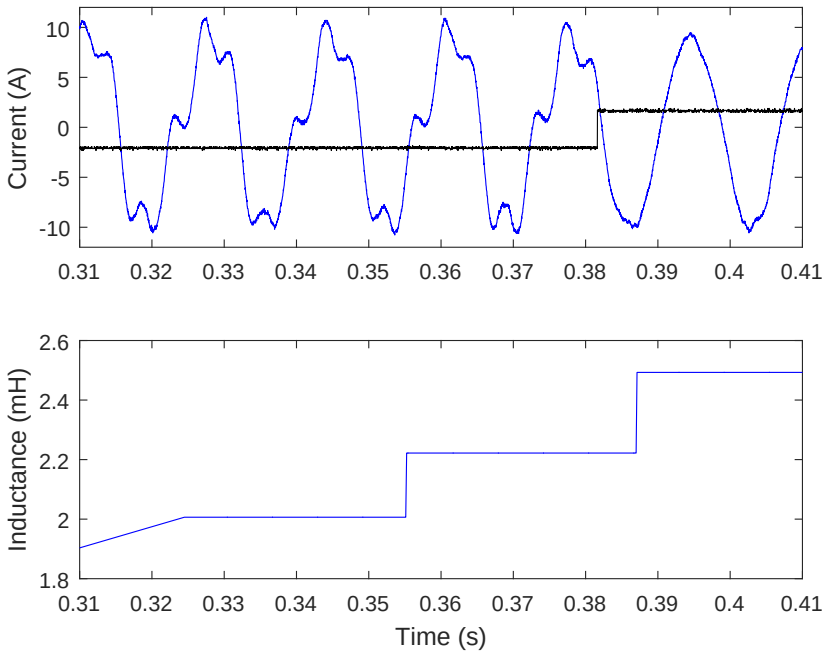

Figure 46: The effect of adaptive control (zoomed).

The adaptive controller operated properly by recovering the weakened current waveforms and thus adapting the whole inverter control system to the increased grid inductance. The extra inductance was connected at 0.1 s and the PLL parameters were adaptively switched at 0.38 s. Hence, it took 0.28 s from adaptive controller to react to the increased grid inductance. Most significant part of that time was due to rising time (0.22 s) of the inductance value when averaged results were applied. Averaged results are nevertheless more reliable for adaptive controller than non-averaged results. The internal delay of the adaptive controller was 0.06 s.

Avoiding Instability

The adaptive control system was tested when 5 mH extra inductor was suddenly connected in series to the grid side. That represents very weak grid conditions where the impedance mismatches possibly occur. The output current FFT in the same situation with 167 Hz PLL is shown Fig. 40 and the similar unstable currents are predicted to occur before the PLL crossover is adaptively decreased to 20 Hz. At the beginning grid has a low inductance value and thus the 167 Hz PLL is applied.

Fig. 47 shows the phase A output current, inductance measurement and the control signal (black line) of the adaptive control system at the time of significantly increased grid inductance. Rising edge of the control signal decreases the PLL crossover from 167 Hz to 20 Hz. At 0.07 s the 5 mH extra inductance is connected. As can be seen from the figure the output current is directly weakened and the waveform between 0.07 s and 0.33 s seems to be unstable because the sinusoidal shape of the current is weakening during that time and the error is not representing any harmonic of the grid. At 0.33 s the control signal has rising edge and the PLL crossover is decreased to 20 Hz. The waveform is directly recovered to the sinusoidal form although just before that the the sinusoidal form was almost completely lost. Hence, the adaptive control recovers stability of the interconnection point.

The rising time to the 2 mH in the inductance measurement result is approx. 0.2 s and the internal delay of the adaptive controller is 0.6 s. In total it took 0.26 s from adaptive controller to react to 5 mH increase in the grid impedance which is faster than in case where 3 mH increase in grid inductance value was studied. This is because the same limit of grid inductance (2 mH) was applied to adaptive controller to react increased grid inductance. The averaged result rising time to the 2 mH is faster when more inductive grid is measured. More inductive grid leads to impedance-based instability

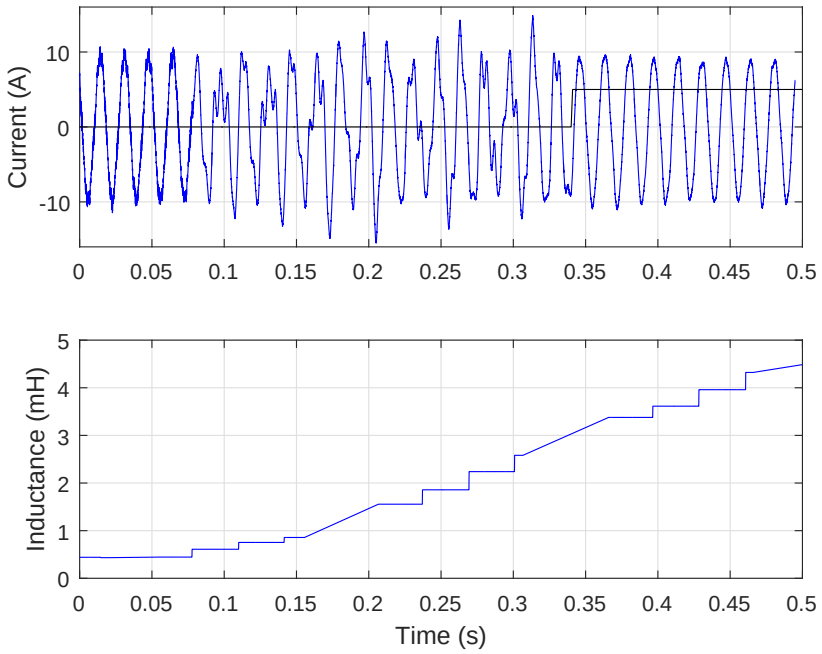

Figure 47: Adaptive control result and grid impedance measurement when current is becoming unstable.

in connection point with inverter and thus the reaction time of the adaptive controller is more critical than in case where only the harmonics is included to inverter output currents. The unstable currents activates the inverter protection system which disconnects the inverter off the load (grid) or source (PV-generator) [41]. The adaptive control should react faster than the inverter protection system to avoid disconnection and ensure continuous power flow. Hence, it is good feature of the adaptive control system to react faster to the more inductive grid.

The adaptive controller operates properly when impedance-based instability occurs in the connection point of the inverter and grid. The inverter control system is adapted to significant increase of grid impedance by decreasing the PLL crossover frequency. PLL dynamics affects q-component of the inverter output impedance and decreasing the crossover of PLL the inverter output impedance is shaped to be suitable with very inductive grid. The adaptive controller also reacts to the instability faster than protection system of the inverter and thus the disconnection from the grid is avoided.

Limit of the higher crossover of the PLL should also be considered. For example when PLL with 200 Hz crossover was applied and similar test was performed by suddenly connecting the 5 mH extra inductance to the grid

side, the protection of the inverter disconnected the inverter off the grid. The impedance mismatches in the connection point of the inverter and grid produced faster increasing unstable current and hence the inverter protection system reacted to instability faster than the adaptive controller. The oscillation based on the impedance mismatches is complex to model and contain several uncertainties and thus the limit for higher crossover of the PLL was adjusted to 167 Hz by experimental tests. Possibilities of even higher extra inductance values than 5 mH should also be taken to account in further research.

6 Conclusion

There is global care of the climate change and thus the energy trend will be based on the environmentally friendly renewable energy production. Renewable energy resources are most often connected to the power grid through inverters. Because of the new energy trend the conventional big synchronous generators will be replaced by distributed renewable energy production which is more flexible but also produce faster changes in distribution system such as power grid. In future the inverters should maintain the power quality of the distribution system in varying operating conditions. Thus there is demand to develop new control ideas for inverters in order to adapt in varying grid conditions and ensure power quality.

Varying grid conditions affects the inverter control system because conventional controllers are designed for one specific operating point. When there is significant changes in operating conditions the inverter control system does not operate properly therefore causing weakened power quality and even instability. One idea is to develop control system which adapts the actual control system to changed operating conditions. This is called as adaptive control. Adaptive control requires measured parameter that describes the current operating conditions.

Grid-connected inverter sees the power grid as impedance. The interface between inverter and power grid can be considered as equivalent source-load subsystem where inverter acts as source and grid as load. The stability of this kind of interface is considered by impedance-based stability analysis in which stability is investigated by considering the impedance ratio. Stability analysis considers the inverter by its output impedance which is affected by characteristics of the implemented control system. The grid impedance is noticed to contain resistance and inductance in low frequencies where the inductance value is varying. The grid inductance varies in changing grid conditions and is shown to describe grid conditions efficiently.

Inverter control system includes phase-locked-loop (PLL) in order to synchronize inverter output currents with the grid voltages. PLL affects significantly to the inverter output impedance, thus, fast dynamics of the PLL leads to power quality problems or even instability when grid inductance increases. This makes PLL controllers attractive target for applying adaptive control based on the grid inductance. Hence, the PLL dynamics can be made faster when grid has low inductance value and should be limited when inductance is increasing to avoid instability.

The system is investigated using power-hardware-in-the-loop (PHIL) tests where the control system is implemented as simulation model and thus the actual hardware controllers are executed by real-time simulator. Hence, the actual inverter is tested and the control system is implemented as simulation which provides fast testing for new control ideas. The simulation model includes adaptive control system that changes parameters of the PLL to provide as fast dynamics as possible based on the grid inductance. The grid impedance is measured continuously based on the maximum length binary sequence (MLBS) injections. MLBS-based measurement system can be implemented thus that the inverter itself produces injection signal to its output current and measure grid impedance. From continuous impedance measurements the grid impedance can be calculated continuously and fed to the adaptive control which adjusts the PLL parameters suitable to current operating conditions.

This thesis has presented adaptive control method for grid-connected inverters. The adaptive control is based on the continuous measurements of grid impedance with the use of MLBS injections which do not require any external measurement device because the measurements can be performed by using only inverter and control system of it. The inductive component of the grid impedance is observed to vary in different grid conditions and thus it is effective parameter to describe operating conditions for the adaptive control system. The implemented control system adapts the PLL parameters by gain scheduling method to provide as fast dynamics as possible in current operating conditions. The effects of the adaptive controlled PLL to the power quality is studied as PHIL-tests in this thesis. The presented method is proven to improve grid currents from harmonic content and avoid instability in changing operating conditions.

References

[1] Bose B. K. Global energy scenario and impact of power electronics in 21st century. *IEEE Transactions on Industrial Electronics*, 60(7):2638–2651, July 2013.

[2] Enslin J. H. R. and Heskes P. J. M. Harmonic interaction between a large number of distributed power inverters and the distribution network. In *Power Electronics Specialist Conference, 2003. PESC '03. 2003 IEEE 34th Annual*, volume 4, pages 1742–1747 vol.4, June 2003.

[3] Roinila T., Luhtala R., Reinikka T., Messo T., Aapro A., and Sihvo J. dspace implementation for real-time stability analysis of three-phase grid-connected systems applying mlbs injection. In *9th EUROSIM Congress on Modelling and Simulation, EUROSIM2016*, Sept 2016.

[4] Jessen L. and Fuchs F. W. Modeling of inverter output impedance for stability analysis in combination with measured grid impedances. In *2015 IEEE 6th International Symposium on Power Electronics for Distributed Generation Systems (PEDG)*, pages 1–7, June 2015.

[5] Roinila T., Vilkko M., and Sun J. Online grid impedance measurement using discrete-interval binary sequence injection. *IEEE Journal of Emerging Selected Topics In Power Electronics*, 2(4):985–993, 2014.

[6] Suntio T. *Dynamic Profile of Switched-Mode Converter*. Wiley-VCH, 2009.

[7] Godfrey K.R. *Perturbation Signals for System Identification*. Prentice Hall, UK, 1993.

[8] Luhtala R. Rapid high-frequency measurements of electrical circuits by using frequency mixer and pseudo-random sequences. Bachelor's thesis, Tampere University of Technology, 2016.

[9] Roinila T. *Fast Frequency Response Measurement Techniques in Analyzing the Dynamics of Switched-Mode Power Supplies*. PhD thesis, Tampere University of Technology, 2010.

[10] Roinila T., Vilkko M., and Sun J. Broadband methods for online grid impedance measurement. In *Energy Conversion Congress and Exposition (ECCE), 2013 IEEE*, pages 3003–3010, Sept 2013.

[11] Monti A., Santi E., Dougal R. A., and Riva M. Rapid prototyping of digital controls for power electronics. *IEEE Transactions on Power Electronics*, 18(3):915–923, May 2003.

[12] Marjanen M. Design and implementation of an induction motor drive test bench. Master of science thesis, Tampere University of Technology, 2015.

[13] Duesterhoeft W., Schulz M. W., and Clarke E. Determination of instantaneus currents and voltages by means of alha, beta and zero components. *Transactions of the American Institute of Electronical Engineers*, 70:1248–1255, 1951.

[14] Teodorescu R., Liserre M., and Rodriguez P. *Grid Synchronization in ThreePhase Power Converters*. Wiley-IEEE Press, 2011.

[15] Park R. H. and Prakash J. Two reaction theoru of synchronous machines. *AKEE Transactions*, 48:716–730, 1929.

[16] Messo T., Aapro A., and Suntio T. Generalized multivariable small-signal model of three-phase grid-connected inverter in dq-domain. In *2015 IEEE 16th Workshop on Control and Modeling for Power Electronics (COMPEL)*, pages 1–8, July 2015.

[17] Hirokazu E. Akagi H. and Aredes M. *Instantaneous power Theory and Applications to Power Conditioning*. Wiley-IEEE Press, 2007.

[18] Dorf R.C. and Bishop R.H. *Modern Control Systems*. Prentice-Hall, 2000.

[19] Messo T., Jokipii J., Puukko J., and Suntio T. Determining the value of dc-link capacitance to ensure stable operation of a three-phase photovoltaic inverter. *IEEE Transactions on Power Electronics*, 29(2):665–673, Feb 2014.

[20] Aapro A. Modeling dynamics of photovoltaic inverter with lcl-tepe grid filter. Mastr of science thesis, Tampere University of Technology, 2014.

[21] Emami-Naeini A. Franklin G. F., Powell J. D. *Feedback Control of Dynamic Systems*. Pearson Prentice Hall, 2010.

[22] Pathiran A. R. and Prakash J. Design and implementation of a model-based pi-like control scheme in a reset configuration for stable single-loop systems. *The Canadian Journal of Chemical Engineering*, 92:1651–1660, August 2014.

[23] Messo T., Jokipii J., and Suntio T. Minimum dc-link capacitance requirement of a two-stage photovoltaic inverter. In *2013 IEEE Energy Conversion Congress and Exposition*, pages 999–1006, Sept 2013.

[24] Cespedes M. and Sun J. Adaptive control of grid-connected inverters based on online grid impedance measurements. *IEEE Transactions on Sustainable Energy*, 5(2):516–523, April 2014.

[25] Reznik A., Simes M. G., Al-Durra A., and Muyeen S. M. Lcl filter design and performance analysis for grid-interconnected systems. *IEEE Transactions on Industry Applications*, 50(2):1225–1232, March 2014.

[26] Kraus J. D. and Fleisch D. A. *Electromagnetics With Applications*. WCB/McGraw-Hill, 1999.

[27] Cespedes M. and Sun J. Renewable energy systems instability involving grid-parallel inverters. In *Applied Power Electronics Conference and Exposition, 2009. APEC 2009. Twenty-Fourth Annual IEEE*, pages 1971–1977, Feb 2009.

[28] Mao H., Boroyevich D., and Lee F. C. Novel reduced-order small-signal model of three-phase pwm rectifiers and its application in control design and system analysis. In *Power Electronics Specialists Conference, 1996. PESC '96 Record., 27th Annual IEEE*, volume 1, pages 556–562 vol.1, Jun 1996.

[29] Tan A.H. and Godfrey K.R. The generation of binary and near-binary pseudorandom signals: An overview. *Instrumentation and Measurement, IEEE Transactions on*, 51(4):583–588, 2002.

[30] Godfrey K.R. Design and application of multifrequency signals. *Computing and Control Engineering Journal*, 2(4):187–195, jul 1991.

[31] Dash P. P. and Kazerani M. Sensitivity analysis of a current-source inverter-based three-phase grid-connected photovoltaic system. In *2016 IEEE Electrical Power and Energy Conference (EPEC)*, pages 1–8, Oct 2016.

[32] Xu J., Qian Q., Xie S., and Zhang B. Grid-voltage feedforward based control for grid-connected lcl-filtered inverter with high robustness and low grid current distortion in weak grid. In *2016 IEEE Applied Power Electronics Conference and Exposition (APEC)*, pages 1919–1925, March 2016.

[33] Cspedes M. and Sun J. Online grid impedance identification for adaptive control of grid-connected inverters. In *2012 IEEE Energy Conversion Congress and Exposition (ECCE)*, pages 914–921, Sept 2012.

[34] Jokipii J., Messo T., and Suntio T. Simple method for measuring output impedance of a three-phase inverter in dq-domain. In *2014 International Power Electronics Conference (IPEC-Hiroshima 2014 - ECCE ASIA)*, pages 1466–1470, May 2014.

[35] Timbus A. V., Teodorescu R., Blaabjerg F., and Borup U. Online grid measurement and ens detection for pv inverter running on highly inductive grid. *IEEE Power Electronics Letters*, 2(3):77–82, Sept 2004.

[36] Do T. D., Leu V. Q., Choi Y. S., Choi H. H., and Jung J. W. An adaptive voltage control strategy of three-phase inverter for stand-alone distributed generation systems. *IEEE Transactions on Industrial Electronics*, 60(12):5660–5672, Dec 2013.

[37] Aström K. J. and Wittenmark B. *Adaptive Control, 2nd edition*. Addison-Wesley, 1995.

[38] Lu B., Wu X., Figueroa H., and Monti A. A low-cost real-time hardware-in-the-loop testing approach of power electronics controls. *IEEE Transactions on Industrial Electronics*, 54(2):919–931, April 2007.

[39] Ghani Z. A., Hannan M. A., and Mohamed A. Development of three-phase photovoltaic inverter using dspace ds1104 board. In *Research and Development (SCOReD), 2009 IEEE Student Conference*, pages 242–245, Nov 2009.

[40] Deshpande A. P., Chaudhari B. N., and Pande V. N. Design and simulation of back-to-back converter for modern wind energy generation system using dspace. In *Power, Signals, Controls and Computation (EPSCICON), 2012 International Conference on*, pages 1–6, Jan 2012.

[41] Myway Plus Corporation. *Inverter Unit MWINV-9R144 hardware User's Manual*, April 2012.